

Joint diffraction and modeling approach to the structure of liquid alumina

Lawrie B. Skinner,^{1,2,3,4} Adrian C. Barnes,¹ Philip S. Salmon,⁵ Louis Hennet,⁶ Henry E. Fischer,⁷ Chris J. Benmore,³ Shinji Kohara,⁸ J. K. Richard Weber,^{3,4} Aleksei Bytchkov,⁹ Martin C. Wilding,¹⁰ John B. Parise,^{2,11,12} Thomas O. Farmer,¹ Irina Pozdnyakova,⁶ Sonia K. Tumber,⁴ and Koji Ohara⁸

¹*H.H. Wills Physics Laboratory, University of Bristol, Tyndall Avenue, Bristol, BS8 1TL, United Kingdom*

²*Mineral Physics Institute, Stony Brook University, Stony Brook, New York, New York 11794-2100, USA*

³*Advanced Photon Source, Argonne National Laboratory, 9700 South Cass Avenue, Argonne, Illinois 60439, USA*

⁴*Materials Development, Inc., Arlington Heights, Illinois 60004, USA*

⁵*Department of Physics, University of Bath, Bath, BA2 7AY, United Kingdom*

⁶*CNRS-CEMHTI, Université d'Orléans, 1d avenue de la Recherche Scientifique, 45071, Orléans cedex 2, France*

⁷*Institut Laue-Langevin, 6 rue Jules Horowitz, BP 156, F-38042, Grenoble, France*

⁸*Japan Synchrotron Radiation Research Institute (SPring-8/JASRI), 1-1-1 Kouto, Sayo, Hyogo 679-5198, Japan*

⁹*European Synchrotron Radiation Facility, 6 rue Jules Horowitz, BP 220, F-38043, Grenoble, France*

¹⁰*Institute of Mathematical and Physical Sciences, Aberystwyth University, Aberystwyth, Ceredigion SY23 3BZ, United Kingdom*

¹¹*Department of Geosciences, Stony Brook University, Stony Brook, New York, New York 11794-2100, USA*

¹²*Photon Sciences Division, Brookhaven National Laboratory, Upton, New York 11973, USA*

(Received 2 September 2012; revised manuscript received 9 November 2012; published 3 January 2013)

The structure of liquid alumina at a temperature ~ 2400 K near its melting point was measured using neutron and high-energy x-ray diffraction by employing containerless aerodynamic–levitation and laser-heating techniques. The measured diffraction patterns were compared to those calculated from molecular dynamics simulations using a variety of pair potentials, and the model found to be in best agreement with experiments was refined using the reverse Monte Carlo method. The resultant model shows that the melt is composed predominantly of AlO_4 and AlO_5 units, in the approximate ratio of 2:1, with only minor fractions of AlO_3 and AlO_6 units. The majority of Al–O–Al connections involve corner-sharing polyhedra (83%), although a significant minority involve edge-sharing polyhedra (16%), predominantly between AlO_5 and either AlO_5 or AlO_4 units. Most of the oxygen atoms (81%) are shared among three or more polyhedra, and the majority of these oxygen atoms are triply shared among one or two AlO_4 units and two or one AlO_5 units, consistent with the abundance of these polyhedra in the melt and their fairly uniform spatial distribution.

DOI: [10.1103/PhysRevB.87.024201](https://doi.org/10.1103/PhysRevB.87.024201)

PACS number(s): 61.20.Qg, 61.05.cp, 61.05.fm, 61.20.Gy

I. INTRODUCTION

Solid alumina (Al_2O_3) has many applications, e.g., in cements, ceramics, abrasives, and high-temperature crucibles, and has well-known solid-state structures.¹ The melt also has applications in the production of large sapphire single crystals^{2–6} and in analyzing the behavior of aluminum-fueled rocket motor effluents.^{7–9} However, the very high melting point temperature of alumina ($T_m = 2327(6)$ K, Ref. 10) has impeded the study of the liquid state, for which many details about its atomic structure and physical properties remain unknown. For example, the reported densities of liquid alumina measured at the melting point vary over a 15% range,^{11–22} but this parameter is essential for establishing reliable structural models. A key problem in many of these investigations is finding a container that is able to withstand high temperatures without reacting with the melt. In this work, the problem is circumvented by employing containerless aerodynamic–levitation and laser-heating techniques.²³

The structure of liquid alumina is also of interest because Al_2O_3 forms a large component of the geologically relevant (Mg/Fe/Ca) aluminosilicates, which account for a significant proportion of Earth's mantle and are present in magma.^{24,25} These materials have received much attention, as they exhibit significant structural and physical property changes at the extreme conditions found within Earth.^{26–29} Alumina is also

the major component in the Y_2O_3 – Al_2O_3 system, which has recently been the subject of debate regarding the observation of an isocompositional liquid–liquid phase transition.^{30–33} It has also been proposed from molecular dynamics (MD) simulations that pure alumina is a candidate for exhibiting a first-order liquid–liquid transition,³⁴ although further investigations indicate a continuous change in structure with increasing pressure.^{35–38} Several of the important thermophysical properties of liquid alumina, such as its viscosity,³⁹ surface tension,³⁹ heat capacity,²² enthalpy of fusion,²² electrical conductivity,⁴⁰ longitudinal speed of sound,⁴¹ and emissivity,⁴² are described elsewhere.

The thermodynamically stable phase of crystalline alumina α - Al_2O_3 is built from octahedral AlO_6 motifs,¹ and the density decrease on melting is ~ 20 – 24% .^{14,43} In metastable crystalline phases, the aluminum coordination environment is usually octahedral or tetrahedral.¹ The existence of a predominantly tetrahedral liquid structure has been found from x-ray diffraction,^{44–47} neutron diffraction,⁴⁸ and high-temperature nuclear magnetic resonance (NMR) experiments.^{49–52} The latter directly probe the environment of the Al atoms, and the observed chemical shifts are consistent with an average Al–O coordination number (i.e., the average number of O atoms around a given Al atom) of ~ 4.5 – 4.8 , the measurement of a more precise value being limited by the challenging high-temperature sample environment. Computer simulation studies,^{34–38,53–58} and an empirical potential

structure refinement (EPSR)⁵⁹ model of neutron diffraction data,⁴⁸ are consistent with the formation of a range of AlO_x polyhedral units, with x taking the value 3, 4, 5 or 6. However, different studies give a wide range of values for the relative proportions of these polyhedra.^{34–38,48,51,53–56} Indeed, an x-ray diffraction study of liquid Al_2O_3 held in a molybdenum cell at 2363 K found a predominantly octahedral liquid with a mean Al-O coordination number of ~ 5.6 .⁶⁰

In the present work, new x-ray and neutron diffraction measurements on stable liquid alumina at 2400(50) K are reported. The neutron diffraction results were used to estimate the liquid density, which was found to be in good agreement with the density measured in an electrostatic-levitation experiment²² and is near the mean of the densities measured by other aerodynamic-levitation versus noncontainerless methods. The diffraction results are initially compared in detail to those obtained by MD simulations using a variety of pair potentials to test the validity of the models thus prepared.^{38,54,61–63} Often these potentials are parameterized using the properties of crystalline phases, which may or may not be relevant to the high-temperature liquid. We therefore adapt a structural model for the liquid by taking the MD model that is in best agreement with the liquid diffraction data and refining it against those data using the reverse Monte Carlo (RMC) method.⁶⁴ A key aim is to make a realistic model in order to investigate the relative proportions, connectivity, and distortion of the AlO_x polyhedra. For example, if the Al-O and O-Al coordination numbers are denoted by $\bar{n}_{\text{Al}}^{\text{O}}$ and $\bar{n}_{\text{O}}^{\text{Al}}$, then it follows from the definition of these coordination numbers (Sec. II) that the average number of O atoms around a given Al atom $\bar{n}_{\text{O}}^{\text{Al}} = (c_{\text{Al}}/c_{\text{O}})\bar{n}_{\text{Al}}^{\text{O}}$, where c_{Al} and c_{O} denote the atomic fractions of Al and O, respectively. Hence, if Al_2O_3 is a predominantly tetrahedral liquid (i.e., $\bar{n}_{\text{Al}}^{\text{O}} = 4$), then $\bar{n}_{\text{O}}^{\text{Al}} = (2/3) \times 4 = 8/3$; i.e., each oxygen atom is shared among an average of 2.67 AlO_4 units. This means that a purely corner-connected tetrahedral structure cannot be supported without triclustering three AlO_4 units through a single oxygen corner, as is observed in aluminate glasses.⁶⁵ If the oxygen atoms can only be twofold or threefold coordinated to aluminum atoms, then the ratio of the number of these twofold to threefold coordinated oxygen atoms is 1:2 for liquid Al_2O_3 .⁶⁵ Such issues must be taken into account to assure that a given model is realistic.

The manuscript is organized as follows. The essential diffraction theory is given in Sec. II, and the experimental and modeling methods are detailed in Sec. III. The results obtained from the diffraction and simulation methods are presented in Sec. IV, where they are compared to those obtained from MD simulations using several sets of pair potentials, and the RMC model is then prepared. The final results are discussed in Sec. V, where particular attention is paid to the nature of the polyhedra and their connectivity. The description of the liquid thus provided does not, in general, imply long-lived structural configurations but represents, instead, an ensemble average of local quasi-instantaneous configurations. This is in keeping with a diffraction experiment in which each x-ray or neutron samples the structure of a liquid within its coherence volume, and a diffraction pattern is built up as an accumulation of such snapshots.⁶⁶ Conclusions are drawn in Sec. VI.

II. THEORY

The coherent scattered intensity measured in a neutron or x-ray diffraction experiment on liquid alumina yields the total structure factor⁶⁶

$$S(Q) = 1 + \frac{1}{|\langle w(Q) \rangle|^2} \sum_{\alpha} \sum_{\beta} c_{\alpha} c_{\beta} w_{\alpha}^{*}(Q) w_{\beta}(Q) [S_{\alpha\beta}(Q) - 1], \quad (1)$$

where $S_{\alpha\beta}(Q)$ is a Faber-Ziman partial structure factor, Q denotes the magnitude of the scattering vector, and c_{α} is the atomic fraction of chemical species α . In general, $w_{\alpha}(Q)$ is a complex number ($*$ denotes a complex conjugate) and represents, for chemical species α , either the Q -independent coherent neutron scattering length (denoted by b_{α}) or the x-ray atomic form factor plus dispersion terms (denoted by $f_{\alpha}(Q)$), which has a strong Q dependence. $|\langle w(Q) \rangle|^2 = \sum_{\alpha} \sum_{\beta} c_{\alpha} c_{\beta} w_{\alpha}^{*}(Q) w_{\beta}(Q)$ is chosen such that the weighting factors for $S_{\alpha\beta}(Q)$ sum to unity for all Q values for either the neutron total structure factor $S^{\text{N}}(Q)$ or the x-ray total structure factor $S^{\text{X}}(Q)$. The neutron scattering lengths for Al and O take real values of $b_{\text{Al}} = 3.449(5)$ and $b_{\text{O}} = 5.805(4)$ fm.⁶⁷ Independent neutral atomic x-ray form factors $f_{\text{Al}}(Q)$ and $f_{\text{O}}(Q)$ were taken from Ref. 68. Any effect on $f_{\alpha}(Q)$ from local bonding is expected to be significant only at $Q < 2 \text{ \AA}^{-1}$ in the measured $S^{\text{X}}(Q)$ function, where valence electrons have their largest effect.

The Fourier transform of $S_{\alpha\beta}(Q)$ gives the partial pair-distribution function $g_{\alpha\beta}(r)$, where r is a distance in real space, while the Fourier transforms of $S^{\text{X}}(Q)$ and $S^{\text{N}}(Q)$ give the total pair-distribution functions $G^{\text{X}}(r)$ and $G^{\text{N}}(r)$, respectively.⁶⁶ The mean coordination number of atoms of type β , contained in a volume defined by two concentric spheres of radii r_{min} and r_{cut} centered on an atom of type α , is given by

$$\bar{n}_{\alpha}^{\beta} = 4\pi\rho c_{\beta} \int_{r_{\text{min}}}^{r_{\text{cut}}} r^2 g_{\alpha\beta}(r) dr \quad (2)$$

where ρ is the atomic number density. In practice, a neutron or x-ray diffractometer can measure only over a finite Q range, which starts at Q_{min} and ends at Q_{max} , and a modification function $M(Q, \Delta(r))$ is often used to militate against the appearance of Fourier transform artifacts such that the total pair-distribution function is written as

$$G^{\text{X/N}}(r) = 1 + \frac{1}{2\pi^2\rho r} \int_{Q_{\text{min}}}^{Q_{\text{max}}} M(Q, \Delta(r)) Q \times [S^{\text{X/N}}(Q) - 1] \sin(Qr) dQ. \quad (3)$$

Simple modification functions, such as the Lorch function,^{69–72} depend only on Q and typically reduce truncation oscillations at the expense of broadening the sharpest features in real space. In this work, we follow the method of Soper and Barney⁷¹ and vary the strength of the modification function for each portion of real space using the modified Lorch function

$$M(Q, \Delta(r)) = \frac{3}{[Q\Delta(r)]^3} \{ \sin[Q\Delta(r)] - Q\Delta(r)\cos[Q\Delta(r)] \}, \quad (4)$$

where $\Delta(r)$ is a real-space broadening width that can be a function of r . To emphasize the structure at higher- r values,

the real-space total density $D^{X/N}(r) = 4\pi\rho[G^{X/N}(r) - 1]$ or partial density $d_{\alpha\beta}(r) = 4\pi\rho[g_{\alpha\beta}(r) - 1]$ functions are also plotted in this work.⁶⁶

To facilitate a comparison of simulated structures to diffraction data, the $g_{\alpha\beta}(r)$ functions from the MD or RMC simulations were Fourier transformed to obtain the partial $S_{\alpha\beta}(Q)$ patterns using

$$S_{\alpha\beta}(Q) - 1 = \frac{4\pi\rho}{Q} \int_0^{r_{\max}} r[g_{\alpha\beta}(r) - 1] \sin(Qr) dr, \quad (5)$$

where r_{\max} is half the length of the simulation box. The $S_{\alpha\beta}(Q)$ functions thus obtained were combined using Eq. (1) to give an $S(Q)$ function, which was then transformed back into r space using the same procedure as used for the experimental data [Eq. (3)]. This process is particularly important for x-ray data, as it takes into proper account the effect of the Q -dependent atomic form factors on the $G^X(r)$ function. To account for these form factors, the method described by Zeidler *et al.*⁷³ was used to obtain the Al-O coordination number from the x-ray diffraction data.

III. METHODS

A. Diffraction experiment details

Three x-ray diffraction experiments were performed at the European Synchrotron Radiation Facility (ESRF), the Advanced Photon Source (APS), and the Super Photon ring-8 (SPRING-8). A single neutron diffraction experiment was performed at the Institut Laue–Langevin (ILL). In each experiment, the sample was investigated *in situ* during laser-heating and aerodynamic–levitation of ~ 50 mg droplets above a conical nozzle,^{23,74} where the droplets were made from melting alumina of purity 99.99% (ESRF, APS, and ILL) or 99.5% (SPRING-8). Oxygen was present in each of the levitation gases. The incident x-ray or neutron beam was centered on the top half of the sample, above the nozzle of the levitator and in the region where the sample temperature of ~ 2400 K was measured using a pyrometer (IMPAC-IS140 at the ESRF, Chino IRCAS at the APS, IMPAC ISQ5/MB25 at the SPRING-8, or AOIP-7010E at the ILL). The spectral emissivity ε_λ of molten alumina at the pyrometer wavelength λ was estimated using the relation $\varepsilon_\lambda = 4n_\lambda/(n_\lambda + 1)^2$, where n_λ is the corresponding refractive index, which holds if the liquid is opaque and the extinction coefficient is small enough for it to have a negligible effect on the Fresnel reflectance.⁷⁵ For instance, $n_\lambda = 1.744(16)$ when $\lambda = 633$ nm such that $\varepsilon_\lambda = 0.926(3)$.⁴² In our experiments, in order to correct the pyrometer readings to give the sample temperature, a constant emissivity $\varepsilon_\lambda = 0.92$ was assumed for the wavelength range 0.7–1.1 μm , which brackets all of the pyrometers used. This assumption is supported by experiments in which the corrected pyrometer readings displayed a temperature arrest on fusing solid alumina at the known melting point of 2327(6) K.¹⁰ Rotation of the liquid drop by the levitation gas stream resulted in temperature oscillations of approximately ± 20 K during the x-ray and neutron measurements. This variation is consistent with the temperature gradients, which are expected to be up to ± 50 K in the top half of the sample probed by the

x-ray or neutron beam. We note that ± 50 K represents a $\pm 2\%$ variation in the sample temperature of 2400 K, which corresponds to a change in the sample density of about $\pm 0.2\%$ (Ref. 22); i.e., there should be a negligible change in the structure.

The ESRF measurement was performed at the ID11 beamline using x-ray photons of wavelength 0.1222(1) \AA (101.5 keV) and a beam of cross-sectional area 0.4×0.4 mm². A FreLoN 2k16 charge-coupled device detector⁷⁶ was placed perpendicular to the incident beam, 160 mm behind the sample, such that one quarter of the Debye–Scherrer cone was measured. This gave a useable Q range up to 24 \AA^{-1} while maintaining an acceptable Q space resolution. The sample was heated from above and from below by 125 W CO₂ lasers (Synrad Evolution). The sample chamber was not sealed or purged from the atmosphere, and the levitation gas stream was arcal (96.5% Ar, 3.5% O₂). The two-dimensional diffraction patterns were reduced using Fit2D software.⁷⁷ The measured background intensity was subtracted and corrections were made for the detector geometry and efficiency, sample self-attenuation, and Compton scattering using standard procedures.^{66,78}

The SPRING-8 measurement was performed at the BL04B2 beamline using a two-axis diffractometer dedicated to the study of glass, liquid, and amorphous materials.⁴⁶ The intensity of incident x rays was monitored by an ionization chamber filled with Ar gas, and the scattered x rays were detected by a solid-state Ge detector. An incident x-ray wavelength of 0.1093(1) \AA (113.4 keV) was used, giving an accessible Q range of 0.3–24 \AA^{-1} , and the incident beam size was 0.5×0.5 mm². The sample was heated from above using a single 100 W CO₂ laser (Synrad Firestar), and dried air was used as the levitation gas. The data were corrected for background scattering, sample self-attenuation, and Compton scattering using standard procedures.^{46,66}

The APS measurement was performed at the 11-ID-C beamline with an incident x-ray beam of wavelength 0.10804(2) \AA (114.76 keV) and cross-sectional area 0.5×0.5 mm². A Perkin Elmer XRD1621 area detector was centered on the beam stop and placed ~ 400 mm behind the sample. It was calibrated using a polystyrene ball coated with a CeO₂ powder standard and gave a Q range of 0.5–24 \AA^{-1} . The sample was heated from above using a single 400 W CO₂ laser (Synrad Firestar), the sample chamber was not sealed or purged from the atmosphere, and the levitation gas stream was oxygen. To avoid attenuation from the levitator nozzle, only data from the top half of the Debye–Scherrer cone was used for analysis. The correction procedures and programs were the same as those used for the ESRF data.

The ILL experiment was made using the diffractometer D4c (Ref. 79) with an incident neutron wavelength of 0.4981(1) \AA , giving a Q range of 0.4–23.5 \AA^{-1} using the setup described in Ref. 74. The sample was heated from above by two 125 W CO₂ lasers (Synrad Evolution). Background scattering from the levitator nozzle was minimized by shielding with neutron-absorbing boron carbide plates so that only the top half of the sample above the nozzle was exposed to the incident neutron beam. Background scattering from air was minimized by evacuating the sample chamber and refilling it with 99.999% argon. Arcal was used for the levitation gas stream; i.e.,

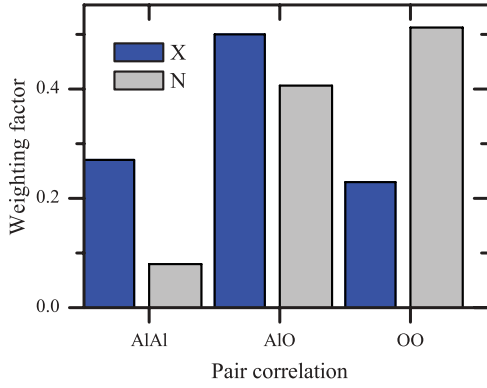


FIG. 1. (Color online) The relative weighting factors as calculated using Eq. (1) for the partial structure factors in x-ray versus neutron diffraction experiments on liquid Al₂O₃. The x-ray and neutron data sets are represented by the dark (blue) and light (gray) histograms, respectively. The x-ray values were calculated for $Q = 0$.

the O₂ level in the sample chamber varied between 0 and 3.5%. The background scattering was therefore monitored at regular intervals. The measured background intensity was subtracted and corrections were made for multiple scattering, sample self-attenuation, and inelastic scattering using standard procedures.⁶⁶

For liquid alumina, the x-ray weighting factors for the Al-Al, Al-O, and O-O Faber-Ziman partial structure factors are ~ 0.270 , 0.499 , and 0.230 , respectively (as evaluated from the form factor values at $Q = 0$), whereas the corresponding neutron weighting factors are 0.080 , 0.406 , and 0.513 , respectively. As illustrated in Fig. 1, the neutron diffraction pattern contains little information on the Al-Al correlations, whereas the x-ray pattern has more information on the Al-Al but less information on the O-O correlations.

B. Simulation details

The majority of the classical MD studies consistent with the measured density range for liquid Al₂O₃ use pair potentials of the form^{38,54,61–63}

$$U_{\alpha\beta}(r) = \frac{z_{\alpha}z_{\beta}e^2}{r} + A_{\alpha\beta} \exp(-r/B_{\alpha\beta}) - \frac{C_{\alpha\beta}}{r^6}, \quad (6)$$

where r is the separation of atom pairs, z_{α} is the charge on an atom of type α , e is the elementary charge, and $A_{\alpha\beta}$, $B_{\alpha\beta}$, and $C_{\alpha\beta}$ are parameters that are usually determined by fitting to vibrational spectra for crystalline materials. A problem with these pair potentials is that they can lead to unphysical attractive forces at small atomic separations.^{62,63} We avoided this problem by adding a $D_{\alpha\beta}/r^{12}$ repulsive term, where $D_{\alpha\beta}$ is the smallest value making the potential and its derivative always positive at low r . The $1/r^{12}$ falloff of this term means that it contributes less than $\sim 1\%$ to the potential when $r > 0.6r_1$, where r_1 is the position of the first peak in the relevant $g_{\alpha\beta}(r)$ function. The D_{AlO} , D_{OO} , and D_{AlAl} values used in the $D_{\alpha\beta}/r^{12}$ correction terms were 12, 200, and 0 eV \AA^{12} , respectively. The other values for the pair potential parameters were taken from the models described by

Hung *et al.*,³⁸ Hoang and Oh,⁵⁴ Du and Corrales,⁶¹ Du *et al.*,⁶² and Winkler *et al.*,⁶³ where in each case, $A_{\text{AlAl}} = C_{\text{AlAl}} = 0$.

MD simulations were made for each pair potential model using the DL_POLY package⁸⁰ on a system containing $N = 6400$ atoms with a time step of 0.001 ps. Each simulation was started from a disordered configuration, where the atoms had been moved at random while satisfying minimum Al-Al, Al-O, and O-O separation distances of 2, 1.3, and 2 \AA , respectively. Using an *NPT* ensemble, the system was then held at a pressure P equal to atmospheric at a temperature $T = 6000$ K for 50 ps and brought down to 2400 K in three equally spaced temperature steps over a period of 100 ps (30 ps at 4800 K, 30 ps at 3600 K, and 40 ps at 2400 K). Finally, *NVT* runs of a 30-ps duration were initiated using the final configuration at the final density found from the *NPT* simulation for each set of pair potentials, where V denotes the volume.

The RMC refinement was initiated from the final configuration obtained from the model that gave best agreement with the measured diffraction patterns. This ensured that the RMC procedure was initiated from a plausible starting structure such that it led to a refinement of that structure, trying to account for effects such as ion polarizability that are not directly accounted for in simple pair potential models. Small maximum moves of 0.025 \AA per atom were used, and the only coordination constraint was that no aluminum atoms were coordinated to less than three or to more than six oxygen atoms in the distance range 0–2.5 \AA , consistent with the results obtained from the MD simulations.

IV. RESULTS

A. Density

The density of liquid Al₂O₃ close to its melting temperature of 2327(6) K (Ref. 10) was estimated from the low- r behavior of the $D(r)$ function measured by neutron diffraction, after it was confirmed that the corrected differential scattering cross-section oscillated about the expected self-scattering level at large Q values.⁶⁶ The result is plotted in Fig. 2, where a comparison is made with the density values obtained from other experimental methods. More comprehensive summaries of the published density data as a function of temperature are given in Refs. 18, 19, and 22.

From Fig. 2, it is clear that the density values from aerodynamically levitated droplets^{19–21} are systematically lower than the values obtained from other measurement techniques.^{11–18} Although levitated samples are free from container contamination, the density is usually obtained by imaging the levitated droplet from above and calculating the volume by assuming a spherical drop. However, due to the opposing forces from gravity and the levitation gas, the aerodynamically levitated drops are often oblate spheroids of volume $(4/3)\pi a^2 b$, where a is the radius in the horizontal plane and b is the distance from the center to a pole along the symmetry axis in a vertical direction. The assumption that $a = b$ therefore leads to an underestimate of the density by a factor $\frac{b}{a}$. The aerodynamic-levitation density measurements are 5–10% lower than other measurements, which is consistent with our observation that most aluminate glasses, prepared by quenching an aerodynamically levitated melt, form oblate spheroids, where a is 5–10% larger than b .

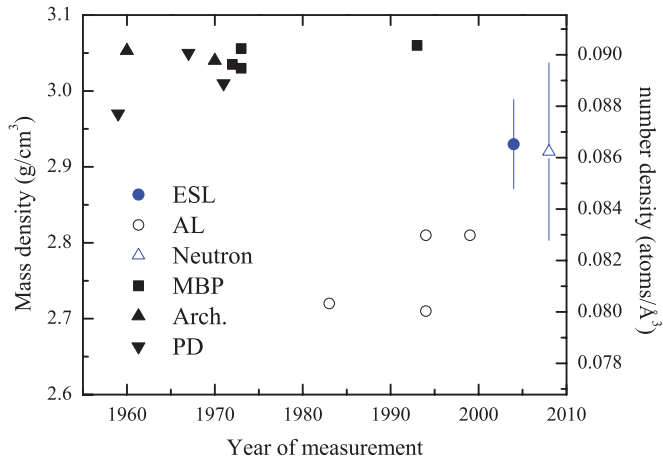


FIG. 2. (Color online) The density of liquid alumina close to its melting temperature of 2327 K as measured with techniques using a pendant drop (PD, solid (black) inverted triangles; Refs. 12–14), Archimedes principle (Arch., solid (black) triangles; Refs. 15 and 16), or maximum gas bubble pressure (MBP, solid (black) squares; Refs. 11, 17, and 18). The results obtained from aerodynamic levitation measurements (AL, open circles; Refs. 19–21) are systematically low, consistent with the assumption of spherical levitated samples (see the text). The measurement made in the present neutron diffraction work (Neutron, open (blue) triangle) is consistent with a measurement made using an electrostatically levitated sample (ESL, solid (blue) circle; Ref. 22).

Our calculated density $\rho = 0.0862(35) \text{ \AA}^{-3}$ is consistent with a recent measurement of $\rho = 0.0863(17) \text{ \AA}^{-3}$ at 2400 K made using an electrostatic levitation setup,²² a containerless method allowing the whole sample to be viewed and promoting sample sphericity by the distribution of surface charge. Both values lie between the densities measured by aerodynamic levitation versus noncontainerless methods.

B. Diffraction data

The three measured $S^X(Q)$ functions, shown in Fig. 3(a), are in close agreement up to $Q = 10 \text{ \AA}^{-1}$, but beyond this limit the ESRF measurement deviates from the other two. This discrepancy, which can be attributed to the detector used in the ESRF experiments, is partially corrected in the back Fourier transform, but some distortion remains. The first peak in $S^X(Q)$ showed no dependence on the oxygen content of the levitation gas stream (3.5% versus $\sim 21\%$ versus 100%). A separate x-ray diffraction experiment made at SPring-8 using the setup described in Sec. III A showed no difference between the structure of molten alumina at 2400 K as measured using either pure argon (99.9999%) or pure oxygen (99.999%) as the levitation gas stream [Fig. 3(g)], in contrast to the relatively low incident energy (20–30 keV) x-ray diffraction work of Krishnan *et al.*,⁴⁷ where the levitation gas was also either pure argon or pure oxygen. The measured $S^N(Q)$ function is compared in Fig. 3(c) to that obtained in a previous neutron diffraction experiment on liquid alumina at 2500 K by Landron *et al.*⁴⁸ and shows a marked improvement in the signal-to-noise ratio. Both functions have the same positions for the first three peaks, but there are marked differences in the heights of the second and third peaks.

The x-ray and neutron total structure factors show a small first peak at $\sim 2.10(2)$ and $1.92(4) \text{ \AA}^{-1}$, respectively [Fig. 3(a) and 3(c)]. The sharp second peak in $S^N(Q)$ at $2.72(2) \text{ \AA}^{-1}$, which manifests itself in $S^X(Q)$ as a small trough, is referred to as the principal peak because it dominates the partial structure factors for liquid alumina (Sec. IV C) and for many other binary systems.^{81–84} The high- Q structure in both the x-ray and the neutron patterns is approximated well by damped sinusoidal oscillations in $Q[S(Q) - 1]$ of periodicity $2\pi/r_1$, where r_1 is the first peak position in $G(r)$.

The $G^X(r)$ functions from the APS and SPring-8 experiments and the $G^N(r)$ function from the ILL experiment are plotted in Fig. 3(b) and 3(d). Although the differences between the APS and Spring-8 data sets are within the experimental error, the latter were chosen for further analysis because they give the closest agreement between the measured $S^X(Q)$ function and the back Fourier transform of $G^X(r)$ after the unphysical oscillations for $r < 1.5 \text{ \AA}$ are set to the $G^X(r \rightarrow 0) = 0$ limit, indicating that the data have been accurately corrected. The x-ray and neutron total pair-distribution functions $G^X(r)$ and $G^N(r)$, respectively, both have an asymmetric first peak at $1.78(1) \text{ \AA}$ or $1.77(1) \text{ \AA}$ with a first minimum at 2.32 \AA or 2.25 \AA , respectively. This peak is assigned to nearest-neighbor Al-O correlations, where the peak position is consistent with the bond distances found for AlO_4 tetrahedra in aluminate liquids and glasses.^{65,85–89} Its integration to $r_{\text{cut}} = 2.25 \text{ \AA}$ gives a coordination number $\bar{n}_{\text{Al}}^{\text{O}} = 4.4(2)$ for both the neutron and x-ray diffraction results, in agreement with the values reported from previous diffraction work.^{44,45,47,48} The Al-O coordination number and first peak asymmetry indicate a significant fraction of longer Al-O bonds, consistent with the presence of AlO_5 and/or AlO_6 polyhedra. Inspection of the partial pair-distribution functions from the MD and RMC models [see, e.g., Fig. 3(f)] shows that there is some overlap of the Al-O correlations with the O-O and Al-Al correlations within the 2–2.5 \AA region and that the minimum in the Al-O partial pair-distribution functions occurs at $\sim 2.5 \text{ \AA}$. The second peak in $G^N(r)$ is at $2.80(2) \text{ \AA}$ and has a high- r shoulder, whereas the second peak in $G^X(r)$ is at $3.1(1) \text{ \AA}$ and is broader. Differences between $G^X(r)$ and $G^N(r)$ are anticipated within this r -space region in accordance with the different Al-Al and O-O weighting factors for the partial pair-correlation functions shown in Fig. 1. Beyond 5 \AA , $G^X(r)$ has little structure, whereas $G^N(r)$ shows decaying sinusoidal oscillations of wavelength $2\pi/Q_{\text{PP}}$, where Q_{PP} is the position of the principal peak, and with a decay length that is related to the width of this peak.⁷² These observations are consistent with the presence of a sharp principal peak in $S^N(Q)$ but an absence of this feature in $S^X(Q)$.

C. Pair potential MD and RMC simulations

The number densities obtained from the NPT simulations at 2400 K using the Du and Corrales,⁶¹ Du *et al.*,⁶² Winkler *et al.*,⁶³ Hoang and Oh,⁵⁴ and Hung *et al.*³⁸ pair potentials were 0.0858(1), 0.0898(1), 0.0855(1), 0.0825(1), and $0.0800(1) \text{ \AA}^{-3}$, respectively, while the pressures obtained from the NVT simulations using these pair potentials with $T = 2400 \text{ K}$ and $\rho = 0.086 \text{ \AA}^{-3}$ were 0.12(3), 1.86(3), 0.04(3), 1.52(4), and 1.35(3) GPa, respectively. The densities from the

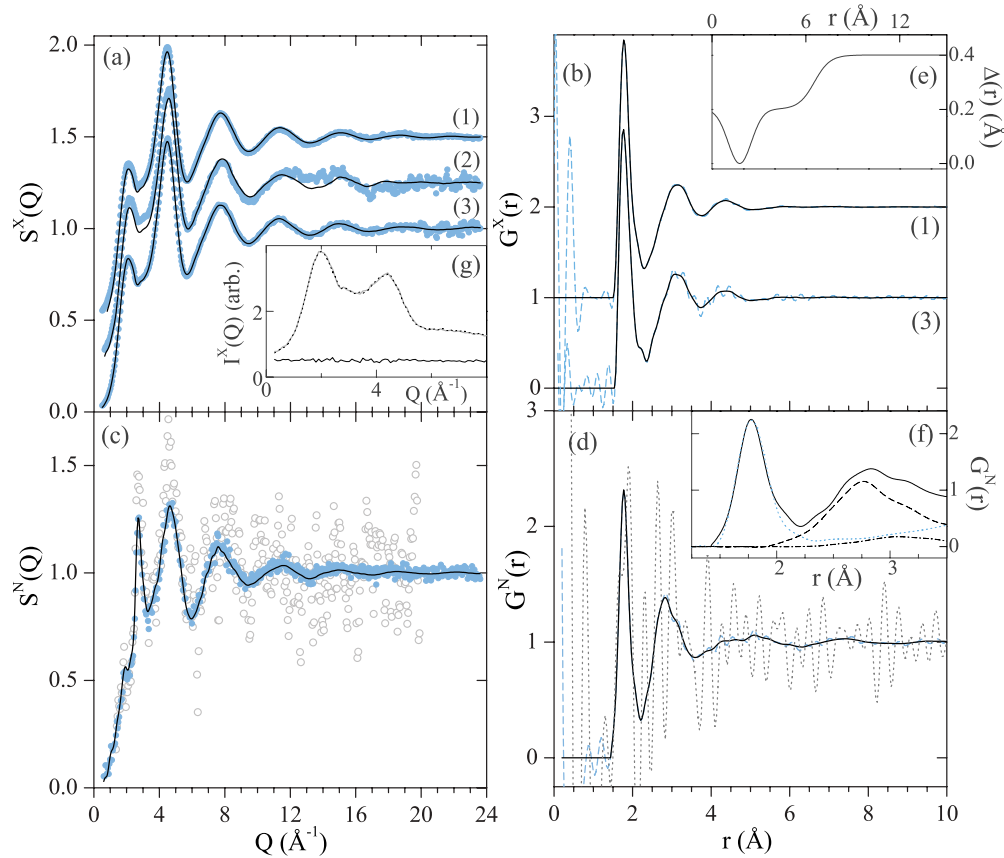


FIG. 3. (Color online) The diffraction results for liquid alumina as measured at 2400(50) K. (a) The solid (blue) circles give $S^X(Q)$ as measured at the (1) APS, (2) ESRF, or (3) SPring-8. The solid (black) curves give the back Fourier transforms of the $G^X(r)$ data sets obtained by applying the modified Lorch function [Eq. (4)], with the unphysical oscillations for $r < 1.5$ Å set to the $G^X(r \rightarrow 0) = 0$ limit. (b) $G^X(r)$ as obtained for (1) the APS and (3) the SPring-8 data by Fourier transforming the corresponding $S^X(Q)$ functions shown in (a) using $Q_{\max} = 23.5$ Å⁻¹ with (solid (black) curve) or without (broken (blue) curve) the application of a modified Lorch function. (c) $S^N(Q)$ as measured at the ILL (solid (blue) circles) or in the work of Landron *et al.* (Ref. 48; open (gray) circles). The solid (black) curve gives the back Fourier transform of $G^N(r)$ for the ILL data shown in (d), as obtained by applying the modified Lorch function with the unphysical oscillations for $r < 1.5$ Å set to the $G^N(r \rightarrow 0) = 0$ limit. (d) The $G^N(r)$ function obtained for the ILL data by Fourier transforming $S^N(Q)$ shown in (c) using $Q_{\max} = 23.5$ Å⁻¹ with (solid (black) curve) or without (broken (blue) curve) the application of a modified Lorch function. The broken (gray) curve gives $G^N(r)$ for the Landron *et al.* (Ref. 48) data as obtained by Fourier transforming $S^N(Q)$ shown in (c) using $Q_{\max} = 19.95$ Å⁻¹. (e) The inset shows $\Delta(r)$ as used in the modified Lorch function [Eq. (4)]. (f) The inset shows the breakdown of the $G^N(r)$ function for the ILL data shown in (d) (solid curve) into its contributions from the weighted Al-O (dotted (blue) curve), O-O (broken curve), and Al-Al (chained curve) partial pair-distribution functions obtained from the RMC refinement. (g) The inset shows the background-corrected intensity $I^X(Q)$ as measured in a SPring-8 x-ray diffraction experiment on molten alumina using either pure oxygen (solid (gray) curve) or pure argon (broken (black) curve) as the levitation gas stream. The difference between the data sets (solid curve) does not reveal significant structural variation caused by the choice of levitation gas.

Du and Corrales⁶¹ and Winkler *et al.*⁶³ models are therefore consistent with the most recent density measurements (Fig. 2), and the pressures obtained using these models are closest to ambient.

The results obtained from these MD simulations using various pair potential models can be separated into those that use formal ion charges^{38,54} and those that use partial ion charges.^{61–63} Within this framework, the results obtained using the Hoang and Oh⁵⁴ formal-charge model and the Du and Corrales⁶¹ partial-charge model agree best with the measured x-ray and neutron diffraction results (Fig. 4). The RMC refinement was initiated from the final configuration of the Du and Corrales⁶¹ model since this gave the best overall agreement with the diffraction data, consistent with a tendency for partial

charges to compensate for “covalent” effects that originate from, e.g., ion polarizability and deformability.^{61,62,90–92} The resultant RMC model shows excellent agreement with the measured neutron and x-ray data sets in both reciprocal and real space (Fig. 4). The small average displacement of 0.17 Å per atom between the final Du and Corrales⁶¹ MD and the final RMC configurations is consistent with the application of a refinement procedure. A comparison is also made in Fig. 4(c) between the measured $S^N(Q)$ function and the results obtained from an EPSR model by Landron *et al.*,⁴⁸ where the latter was made using the noisy neutron diffraction data shown in Fig. 3(c).

The partial structure factors $S_{\alpha\beta}(Q)$ and partial density functions $d_{\alpha\beta}(r)$ from the RMC refinement are compared to

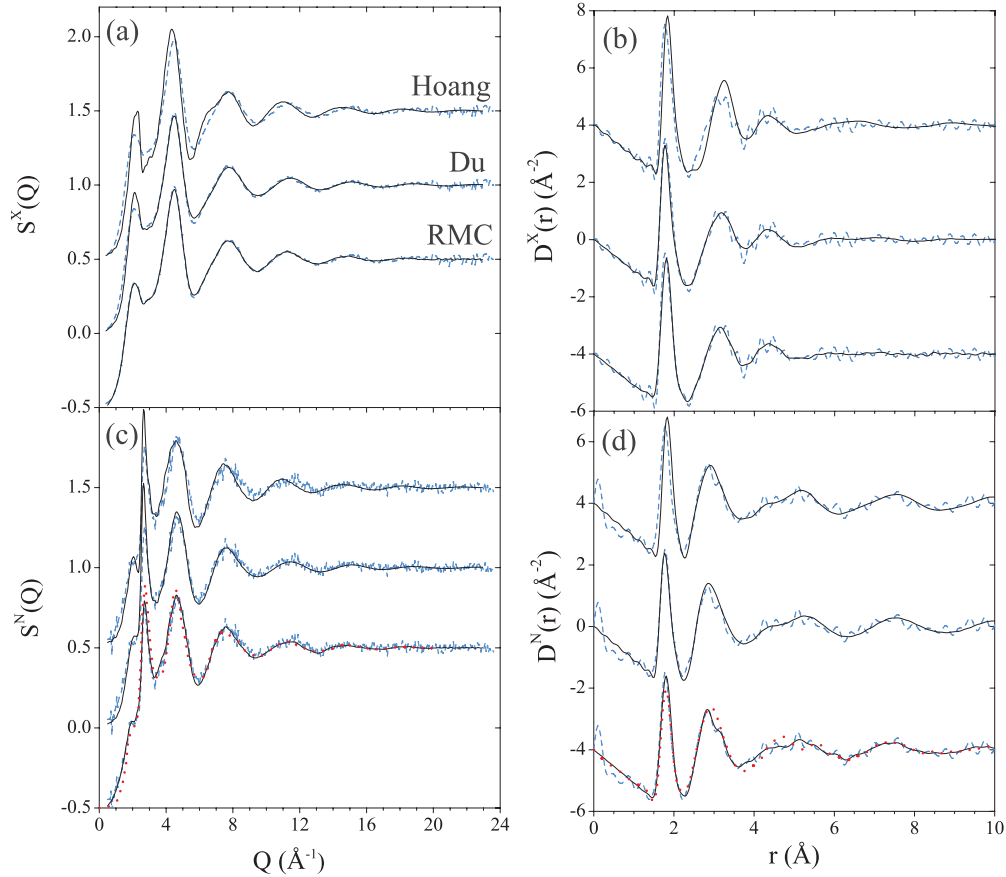


FIG. 4. (Color online) The x-ray and neutron total structure factors $S(Q)$ and total density functions $D(r)$ for liquid Al_2O_3 , where the latter were obtained from $S(Q)$ by applying the modified Lorch function [Eq. (4)] with $Q_{\text{max}} = 23.5 \text{ \AA}^{-1}$. (a) The x-ray total structure factor $S^X(Q)$, (b) the x-ray total density function $D^X(r)$, (c) the neutron total structure factor $S^N(Q)$, and (d) the neutron total density function $D^N(r)$. In each panel, the measured function from the SPring-8 or ILL experiment (broken (blue) curve) is compared to the MD results obtained from the Hoang and Oh (Ref. 54) potentials (top), the Du and Corrales (Ref. 61) potentials (middle), and to the RMC results (bottom), where these modeled results are given by the solid (black) curves. In (c) and (d), the neutron diffraction results are also compared to those obtained from the EPSR model of Landron *et al.* (Ref. 48), for which $\rho = 0.0830(9) \text{ \AA}^{-3}$ (dotted (red) curves).

those obtained from the Du and Corrales⁶¹ model in Fig. 5. The principal peak positions Q_{PP} in reciprocal space and first peak positions in real space $r_{\alpha\beta}$ are summarized in Table I. All of the $S_{\alpha\beta}(Q)$ functions show a sharp principal peak or trough with a position Q_{PP} in the range $2.55\text{--}2.66 \text{ \AA}^{-1}$, which does not manifest itself as a marked feature in the measured $S^X(Q)$ functions because the x-ray weighting factors lead to an almost complete cancellation of $S_{\text{AlAl}}(Q)$ and $S_{\text{OO}}(Q)$ with $S_{\text{AlO}}(Q)$. The $d_{\alpha\beta}(r)$ patterns all show exponentially decaying sinusoidal oscillations at high r of frequency $2\pi/Q_{\text{PP}}$.

TABLE I. The positions of the principal peak in $S_{\alpha\beta}(Q)$ and the first peak in $d_{\alpha\beta}(r)$ for those models found to be most consistent with the measured diffraction data sets. The models of Du and Corrales (Ref. 61) and Jahn and Madden (Ref. 53) are discussed in Secs. IV C and V A, respectively.

| Model | $Q_{\text{PP}} (\text{\AA}^{-1})$ | | | $r_{\alpha\beta} (\text{\AA})$ | | |
|-------------------------------|-----------------------------------|---------|---------|--------------------------------|---------|---------|
| | Al-Al | Al-O | O-O | Al-Al | Al-O | O-O |
| Du and Corrales ⁶¹ | 2.55(1) | 2.60(1) | 2.63(2) | 3.20(2) | 1.76(2) | 2.83(2) |
| Jahn and Madden ⁵³ | 2.64(3) | 2.62(3) | 2.66(2) | 3.14(1) | 1.73(1) | 2.82(2) |
| Present work (RMC) | 2.56(1) | 2.60(1) | 2.63(2) | 3.15(1) | 1.80(1) | 2.82(1) |

V. DISCUSSION

A. Comparison with other MD studies

Liquid Al_2O_3 has also been investigated using MD with models that go beyond simple pair potentials. Studies that are consistent with the measured densities have been reported by Vashishta *et al.*⁵⁸ and by Jahn and Madden.⁵³ In the work by Vashishta *et al.*⁵⁸ on the liquid at 2600 K, $\rho = 0.0830 \text{ \AA}^{-3}$ and the potentials, which included three-body angular constraints, were parameterized using the properties

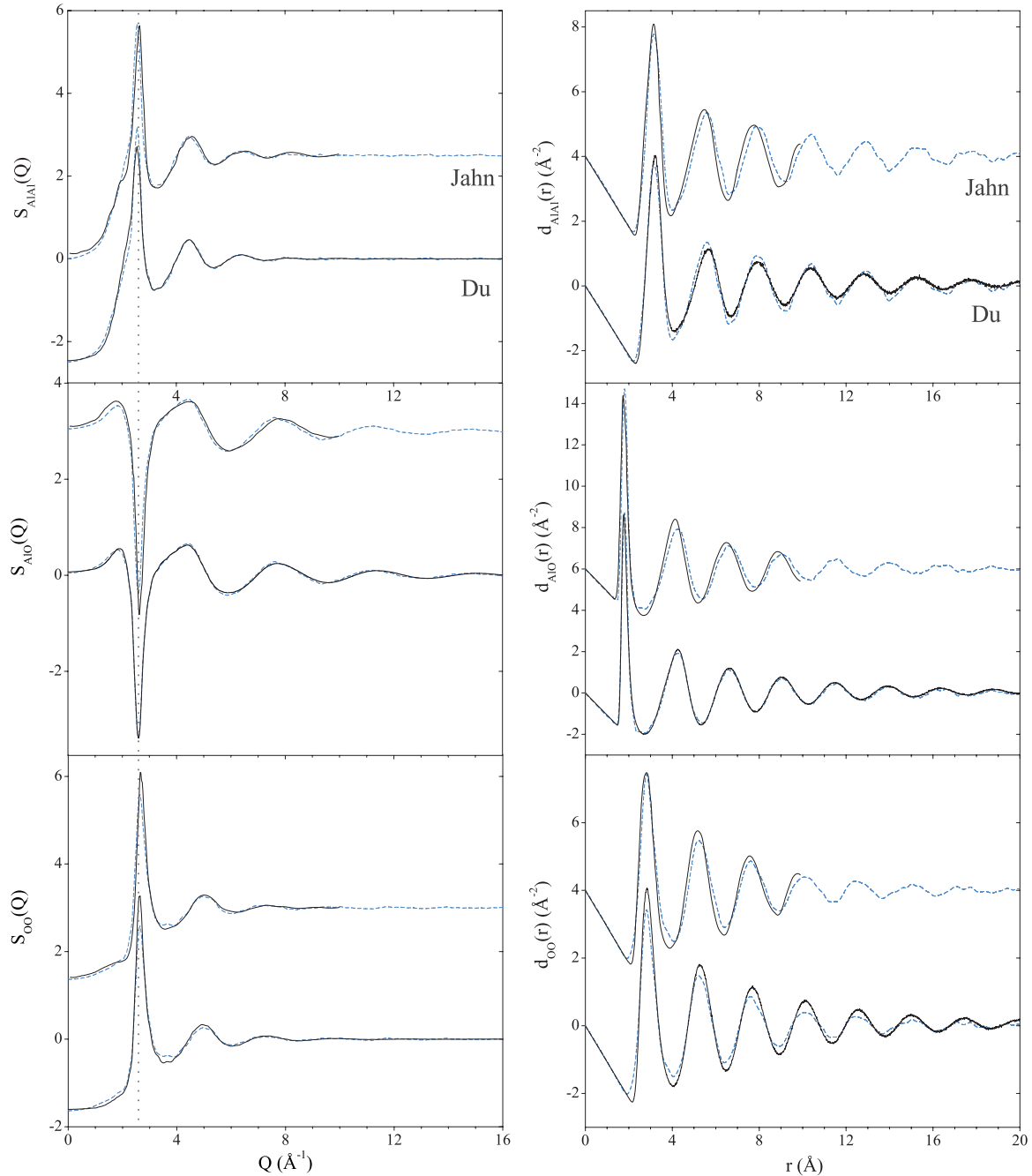


FIG. 5. (Color online) The Faber–Ziman partial structure factors $S_{\alpha\beta}(Q)$ and the partial density functions $d_{\alpha\beta}(r)$. In each panel, the results from the RMC model (broken (blue) curves) are compared to the MD results obtained either by Jahn and Madden (Ref. 53; top) or by using the Du and Corrales (Ref. 61) pair potentials (bottom), where the MD results are given by the solid (black) curves. The broken vertical (gray) line is a guide to the eye for the principal peak position Q_{PP} .

of α - Al_2O_3 . In the work by Jahn and Madden,⁵³ the potentials were parameterized using density functional theory–based electronic structure calculations that included ion polarizability and shape-deformation effects.⁹³ A density of $\rho = 0.0848 \text{ \AA}^{-3}$ at 2350 K was obtained without the application of volume constraints. The x-ray and neutron total structure factors from the Jahn and Madden⁵³ model are in better agreement with the experimental data as shown in Fig. 6. The partial structure factors and partial density functions from this model are compared to the RMC results in Fig. 5.

B. Coordination and connectivity

The first coordination shell from the RMC and other models is relatively ill defined in that the function $g_{\text{AlO}}(r)$ is not equal to zero at the minimum just beyond the first peak [see, e.g., Fig. 3(f)]. This introduces some ambiguity into determining the Al–O coordination number, since it depends on the value chosen for the cutoff distance r_{cut} in Eq. (2). This cutoff distance also affects the number of oxygen atoms found around a given Al atom in the atomic configurations generated by the models; it can therefore change the observed distribution of

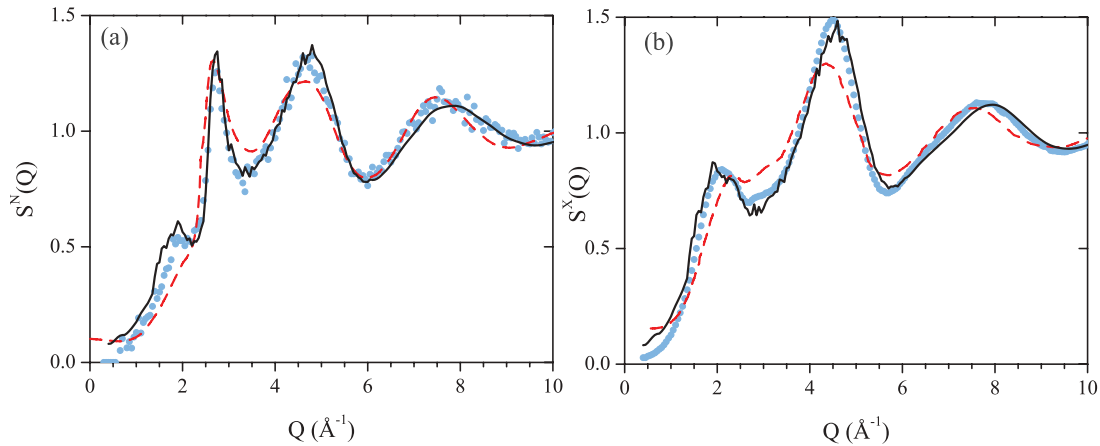


FIG. 6. (Color online) (a) The neutron total structure factor $S^N(Q)$ (solid (blue) circles) and (b) the x-ray total structure factor $S^X(Q)$ (solid (blue) circles) as measured at the ILL and SPring-8, respectively. The data sets are compared to the MD results of Jahn and Madden (Ref. 53; solid (black) curves) and Vashishta *et al.* (Ref. 58; broken (red) curves).

AlO_x species. The first minimum in the $g_{\text{AlO}}(r)$ functions from the RMC model and from the MD models of Jahn and Madden⁵³ and Du and Corrales⁶¹ occurs at ~ 2.5 Å. The relative fractions of AlO_x species ($x = 3, 4, 5$, or 6) obtained using this cutoff distance for the RMC model are compared in Fig. 7(a) to the relative fractions obtained for several other models.^{48,53,54,61,63} The RMC results show a liquid structure that is dominated by AlO_4 and AlO_5 units, consistent with several of the models. A more complete picture of the fraction of AlO_x species obtained from the RMC model by varying r_{cut} is given in Fig. 7(b). For example, the fraction of AlO_4 tetrahedra found for $r_{\text{cut}} = 2.5$ Å increases by $\sim 10\%$ when this cutoff distance is reduced to 2.2 Å, close to the first minimum in $G^N(r)$.

For comparison, sputtered amorphous thin films of Al_2O_3 have been investigated using ^{27}Al triple quantum magic-angle spinning NMR.⁹⁴ The results give an amorphous network made from $55(3)\%$ AlO_4 , $42(3)\%$ AlO_5 , and $3(2)\%$ AlO_6 units. For the liquid at ~ 2400 K, the RMC model (with $r_{\text{cut}} = 2.5$ Å) gives a structure made from $3.5(6)\%$ AlO_3 , $57.5(9)\%$ AlO_4 , $34.7(1.2)\%$ AlO_5 , and $4.3(3)\%$ AlO_6 units. In both cases, AlO_4 and AlO_5 polyhedra constitute the predominant structural motifs and there are only minimal fractions of AlO_6 octahedra.

The relative fractions of OAl_x species ($x = 2, 3$, or 4) from the RMC model obtained using $r_{\text{cut}} = 2.5$ Å are compared in Fig. 7(c) to the relative fractions obtained for several other models.^{48,53,54,61,63} The results show that the majority of oxygen atoms are shared among three AlO_x units. The dependence of the relative fractions of OAl_x species on r_{cut} for the RMC model [Fig. 7(d)] shows that this is the dominant connection type for a range of cutoff distances.

It is instructive to identify the different subspecies in the RMC model. Al4 is used to denote aluminum atoms in units that are coordinated to four or fewer oxygen atoms, Al5 is used to denote aluminum atoms in units that are coordinated to five or more oxygen atoms, O2 is used to denote oxygen atoms that are coordinated to two or fewer Al atoms, and O3 is used to denote oxygen atoms that are coordinated to three or more Al atoms. From Fig. 7, it follows that most of the Al4 , Al5 , O2 , and O3 subspecies correspond to AlO_4 , AlO_5 ,

OAl_2 , and OAl_3 units, respectively. The atomic fractions of the various subspecies are $c_{\text{Al4}} = 0.61(2)c_{\text{Al}}$, $c_{\text{Al5}} = 0.39(2)c_{\text{Al}}$, $c_{\text{O2}} = 0.19(2)c_{\text{O}}$, and $c_{\text{O3}} = 0.81(2)c_{\text{O}}$, respectively.

The coordination numbers of the various aluminum and oxygen subspecies are summarized in Table II. The ratio of the mean number of O3 atoms about a given Al4 atom to the mean number of all O atoms about that Al4 atom, namely, $\bar{n}_{\text{Al4}}^{\text{O3}}:\bar{n}_{\text{Al4}}^{\text{O}}$, shows that $84(1)\%$ of the oxygen atoms in Al4 -type units are shared among three or more polyhedra. Likewise, the ratio $\bar{n}_{\text{Al4}}^{\text{O2}}:\bar{n}_{\text{Al4}}^{\text{O}}$ shows that the remaining $16(1)\%$ of the oxygen atoms in these units are shared between two or fewer polyhedra. By comparison, the ratio $\bar{n}_{\text{Al5}}^{\text{O3}}:\bar{n}_{\text{Al5}}^{\text{O}}$ shows that $91(1)\%$ of the oxygen atoms in Al5 -type units are shared among three or more polyhedra, while the ratio $\bar{n}_{\text{Al5}}^{\text{O2}}:\bar{n}_{\text{Al5}}^{\text{O}}$ shows that the remaining $9(1)\%$ of the oxygen atoms in these units are shared between two or fewer polyhedra.

To investigate the tendency of Al_y -type units ($y = 4$ or 5) to cluster around Al_x -type units ($x = 4$ or 5), a preference factor $f_{\text{Al}_x}^{\text{Al}_y}$ is defined, where

$$f_{\text{Al}_x}^{\text{Al}_y} = \left(\frac{\bar{n}_{\text{Al}_x}^{\text{Al}_y}}{c_{\text{Al}_y}} \right) / \left(\frac{\bar{n}_{\text{Al}_x}^{\text{Al}}}{c_{\text{Al}}} \right). \quad (7)$$

If the Al4 - and Al5 -type units have comparable sizes and are randomly distributed over the Al sites in the system, such that there is no energy penalty in exchanging one subspecies for another, the partial pair-distribution functions for the aluminum subspecies $g_{\text{Al}_x\text{Al}_y}(r)$ will all be equal to $g_{\text{AlAl}}(r)$.⁹⁵ In this case, it follows from Eq. (2) that $\bar{n}_{\text{Al}_x}^{\text{Al}_y}/c_{\text{Al}_y} = \bar{n}_{\text{Al}_x}^{\text{Al}}/c_{\text{Al}}$ such that $f_{\text{Al}_x}^{\text{Al}_y} = 1$. By comparison, if there is a preference for the Al sites around Al_x to be occupied by Al_y -type atoms, then a larger coordination number $\bar{n}_{\text{Al}_x}^{\text{Al}_y}$ is expected such that $f_{\text{Al}_x}^{\text{Al}_y} > 1$. Similarly, a dislike for the Al sites around Al_x to be occupied by Al_y -type aluminum will lead to $f_{\text{Al}_x}^{\text{Al}_y} < 1$.

The preference factors found for the RMC model using the coordination numbers from Table II are $f_{\text{Al4}}^{\text{Al4}} = 1.00(3)$, $f_{\text{Al4}}^{\text{Al5}} = 1.00(4)$, $f_{\text{Al5}}^{\text{Al4}} = 0.96(2)$, and $f_{\text{Al5}}^{\text{Al5}} = 1.06(3)$. They indicate no particular preference for clustering of one type of aluminum subspecies about Al4 -type units but show a

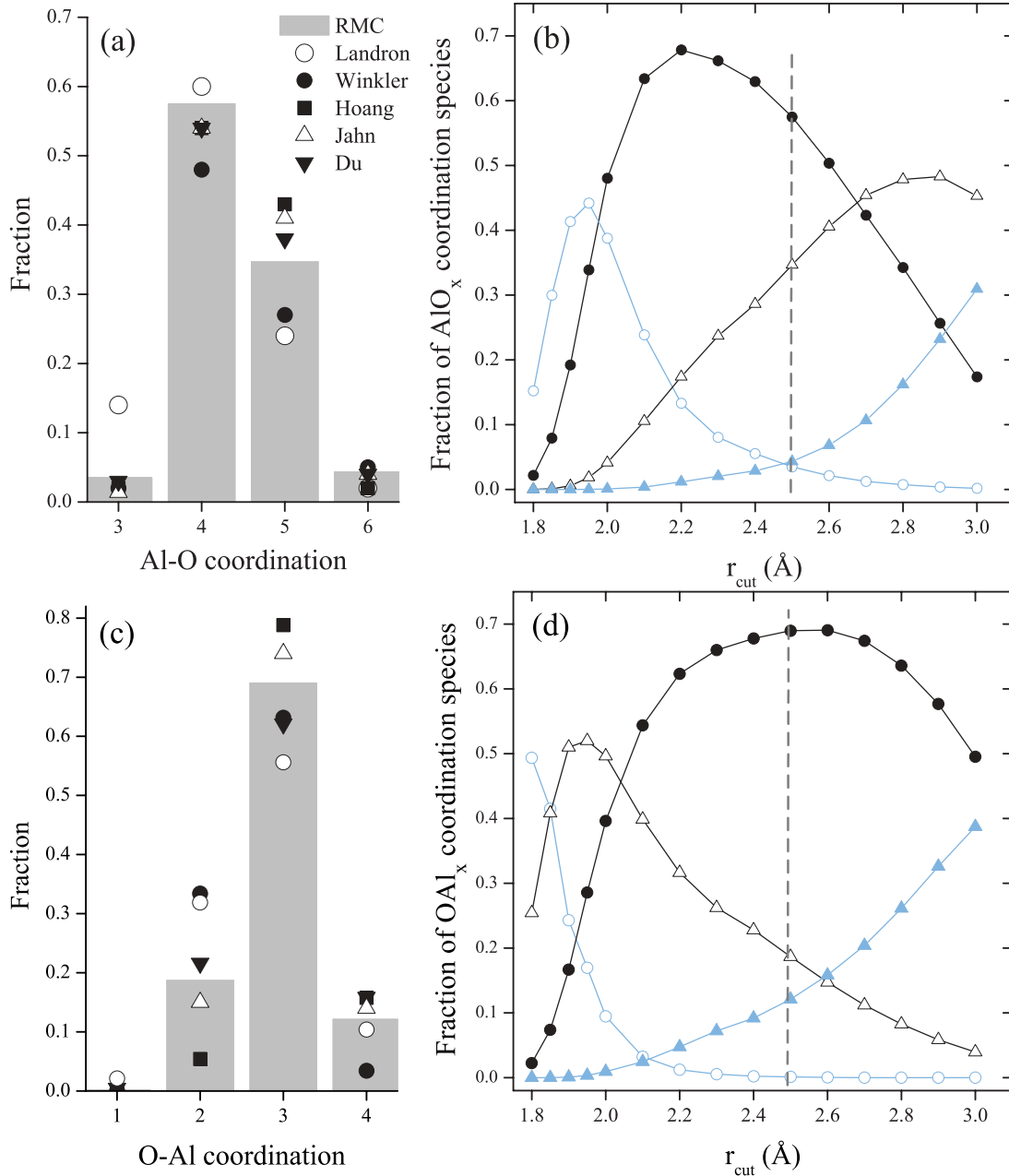


FIG. 7. (Color online) (a) The distribution of AlO_x units ($x = 3, 4, 5$, or 6) as obtained for a cutoff distance $r_{\text{cut}} = 2.5$ Å for the RMC model (gray bars) compared to the models of Landron *et al.* (Ref. 48), Winkler *et al.* (Ref. 63), Hoang and Oh (Ref. 54), Jahn and Madden (Ref. 53), and Du and Corrales (Ref. 61). (b) The dependence of the fractions of AlO_x units on r_{cut} for the RMC model when $x = 3$ (open (blue) circles), $x = 4$ (solid (black) circles), $x = 5$ (open (black) triangles), or $x = 6$ (solid (blue) triangles). (c) The distribution of OAl_x units ($x = 2, 3$ or 4) as obtained for $r_{\text{cut}} = 2.5$ Å for the RMC model (gray bars) compared to the models of Landron *et al.* (Ref. 48), Winkler *et al.* (Ref. 63), Hoang and Oh (Ref. 54), Jahn and Madden (Ref. 53), and Du and Corrales (Ref. 61). (d) The dependence of the fractions of OAl_x units on the cutoff distance r_{cut} for the RMC model when $x = 1$ (open (blue) circles), $x = 2$ (open (black) triangles), $x = 3$ (solid (black) circles), or $x = 4$ (solid (blue) triangles). The vertical broken lines in (b) and (d) correspond to the cutoff distances used for the histograms shown in (a) and (c).

small preference for Al5-type units to connect to other Al5-type units. This observation was checked by treating liquid alumina as a pseudobinary mixture of Al4- and Al5-type units and constructing the Bhatia–Thornton concentration–concentration partial pair distribution function^{95,96}

$$g_{CC}(r) = c_{\text{Al4}}c_{\text{Al5}}[g_{\text{Al4Al4}}(r) + g_{\text{Al5Al5}}(r) - 2g_{\text{Al4Al5}}(r)]. \quad (8)$$

The resultant function is essentially flat and featureless (Fig. 8), consistent with $g_{\text{Al4Al4}}(r) \cong g_{\text{Al5Al5}}(r) \cong g_{\text{Al4Al5}}(r)$ and the ambiguity in defining the polyhedra units, pointing to a fairly uniform distribution of polyhedra over the aluminum sites. There is, however, a small bump in $g_{CC}(r)$ at the first peak position in $g_{\text{Al5Al5}}(r)$, indicating a small preference for like neighbors at this distance. The first peak in $g_{\text{Al5Al5}}(r)$ occurs at a smaller distance than the first peak in $g_{\text{AlAl}}(r)$, consistent

TABLE II. The coordination numbers obtained from the RMC model using cutoff distances r_{cut} of 2.5 Å for the Al-O or O-Al correlations and 4.0 Å for the Al-Al or O-O correlations. The uncertainties were calculated from the variation among 20 configurations. The values of $\bar{n}_{\text{Al4}}^{\text{O}}$ and $\bar{n}_{\text{Al5}}^{\text{O}}$ are not equal to integers, because Al4 denotes Al atoms in both AlO_3 and AlO_4 units while Al5 denotes Al atoms in both AlO_5 and AlO_6 units.

| $\bar{n}_{\text{Al}}^{\text{O}}$ 4.40(4) | | | | $\bar{n}_{\text{Al}}^{\text{Al}}$ 8.85(3) | | | |
|---|---|---|---|---|---|--|---|
| $\bar{n}_{\text{Al4}}^{\text{O}}$ 3.94(2) | | $\bar{n}_{\text{Al5}}^{\text{O}}$ 5.11(2) | | $\bar{n}_{\text{Al4}}^{\text{Al}}$ 8.59(8) | | $\bar{n}_{\text{Al5}}^{\text{Al}}$ 9.15(6) | |
| $\bar{n}_{\text{Al4}}^{\text{O2}}$ 0.64(2) | $\bar{n}_{\text{Al4}}^{\text{O3}}$ 3.30(2) | $\bar{n}_{\text{Al5}}^{\text{O2}}$ 0.45(2) | $\bar{n}_{\text{Al5}}^{\text{O3}}$ 4.65(2) | $\bar{n}_{\text{Al4}}^{\text{Al4}}$ 5.25(12) | $\bar{n}_{\text{Al4}}^{\text{Al5}}$ 3.34(12) | $\bar{n}_{\text{Al5}}^{\text{Al4}}$ 5.37(8) | $\bar{n}_{\text{Al5}}^{\text{Al5}}$ 3.78(11) |
| $\bar{n}_{\text{O}}^{\text{Al}}$ 2.93(3) | | | | $\bar{n}_{\text{O}}^{\text{O}}$ 12.90(2) | | | |
| $\bar{n}_{\text{O2}}^{\text{Al}}$ 2.00(1) | | $\bar{n}_{\text{O3}}^{\text{Al}}$ 3.16(1) | | $\bar{n}_{\text{O2}}^{\text{O}}$ 12.72(4) | | $\bar{n}_{\text{O3}}^{\text{O}}$ 12.93(3) | |
| $\bar{n}_{\text{O2}}^{\text{Al4}}$ 1.38(2) | $\bar{n}_{\text{O2}}^{\text{Al5}}$ 0.62(2) | $\bar{n}_{\text{O3}}^{\text{Al4}}$ 1.67(3) | $\bar{n}_{\text{O3}}^{\text{Al5}}$ 1.49(3) | $\bar{n}_{\text{O2}}^{\text{O2}}$ 2.33(6) | $\bar{n}_{\text{O2}}^{\text{O3}}$ 10.39(5) | $\bar{n}_{\text{O3}}^{\text{O2}}$ 2.43(4) | $\bar{n}_{\text{O3}}^{\text{O3}}$ 10.50(4) |

with the relatively large fraction of edge-sharing configurations between two Al5-type units (Table III). By comparison, the MD model of Hemmati *et al.*³⁴ showed a rise in the Al-Al partial structure factor for AlO_6 units at $Q < 1 \text{ \AA}^{-1}$, suggesting a clustering of AlO_6 octahedra. However, the density for this model (3.97 g cm⁻³) was ~35% higher than the experimental value for the liquid at ambient pressure (Fig. 2), being more representative of the solid phase.

Table III lists the percentages of different polyhedral connections in the RMC model of liquid alumina. The Al x -type units mostly share corners (~83%), but there is also a significant fraction of edge-sharing configurations (~16%). Most of the connections between two Al4-type units are corner-sharing, and as concerns the oxygen atoms in Al4-type units, the fractions joined to one, two, or three other Al4-type

units are 38(1), 46(1), and 15(1)%, respectively. Since most of the Al4-type units correspond to AlO_4 tetrahedra, ~15(1)% of the corners of these units are shared among three AlO_4 tetrahedra; i.e., there are non-negligible numbers of oxygen triclusters. Edge-sharing conformations account for ~1/3 of the connections between two Al5-type units and ~1/6 of the connections among Al4- and Al5-type units. Of the oxygen atoms in Al5-type units, only 14(1)% are shared among three Al5-type units. Since most of the oxygen atoms are threefold coordinated and O3-(Al5)₃ connections are a minority, it follows that the dominant connection type is among three mixed Al4- and Al5-type units, i.e., threefold coordinated oxygen atoms are shared predominantly among one or two AlO_4 units and two or one AlO_5 units.

In summary, the analysis of the RMC-refined MD model gives a picture of a mixed polyhedral liquid, where there are ~2/3 AlO_4 units and ~1/3 AlO_5 units and where the majority of oxygen atoms are threefold coordinated to Al atoms (Fig. 7). The two polyhedral types predominantly share corners, but there are substantial numbers of edge-sharing connections, where ~1/3 of the AlO_5 units share edges with other AlO_5 units and ~1/6 of the AlO_5 units share edges with AlO_4 units (Table III). Since the ratio $\bar{n}_{\text{Al4}}^{\text{O2}}:\bar{n}_{\text{Al4}}^{\text{O}}$ is 16(1)%, whereas the ratio $\bar{n}_{\text{Al5}}^{\text{O2}}:\bar{n}_{\text{Al5}}^{\text{O}}$ is 9(1)%, it follows that the AlO_4 units are more likely to be connected by twofold coordinated oxygen atoms

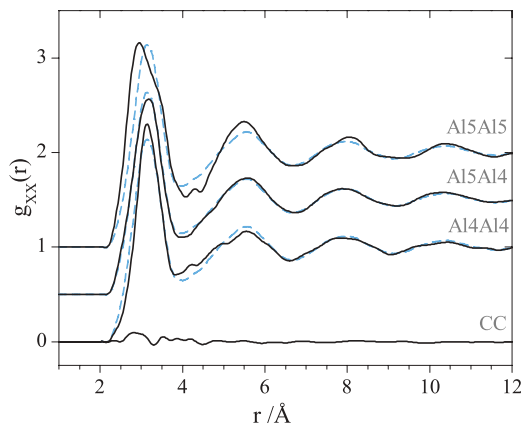


FIG. 8. (Color online) The Bhatia-Thornton concentration-concentration partial pair-distribution function $g_{CC}(r)$ as constructed from $g_{\text{Al4Al4}}(r)$, $g_{\text{Al4Al5}}(r)$, and $g_{\text{Al5Al5}}(r)$ using Eq. (8) after treating liquid alumina as a pseudobinary mixture of Al4- and Al5-type units (see the text). For comparison, each $g_{\text{Al}x\text{Al}y}(r)$ function is compared to the Al-Al partial pair-distribution function $g_{\text{AlAl}}(r)$ as constructed before a subdivision into Al4- and Al5-type units is made (broken (blue) curves).

TABLE III. The percentages of corner-, edge-, and face-sharing Al-centered polyhedra in the RMC model of liquid Al_2O_3 . The polyhedra were subdivided into Al4- or Al5-type units using a cutoff distance $r_{\text{cut}} = 2.5 \text{ \AA}$ (see the text), and the percentages of corner-, edge-, and face-sharing Al4-Al4, Al4-Al5, and Al5-Al5 connections are also listed.

| | Corner | Edge | Face |
|---------|----------|---------|--------|
| Al-Al | 83.4(1) | 16.1(1) | 0.6(1) |
| Al4-Al4 | 95.72(4) | 4.28(4) | — |
| Al4-Al5 | 83.9(2) | 16.0(2) | 0.1(1) |
| Al5-Al5 | 61.8(4) | 35.6(5) | 2.5(2) |

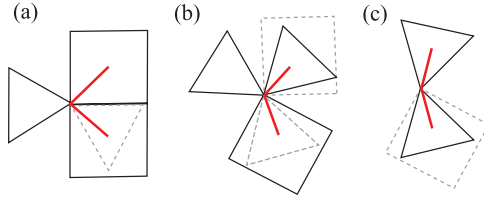


FIG. 9. (Color online) Schematic to show the most prevalent polyhedra and their connectivity in liquid alumina, where solid or broken squares represent AlO_5 polyhedra and solid or broken triangles represent AlO_4 tetrahedra. The edge- and corner-sharing configurations shown in (a) and (c) are less abundant than the configurations shown in (b), where a corner is shared among three polyhedra. The most common arrangement found in the RMC model corresponds to a threefold coordinated oxygen atom which links the corners of one or two AlO_4 units and two or one AlO_5 units. The thick (red) lines are drawn as a guide to the interpolyhedral Al-O-Al angle for each bonding scheme.

than are AlO_5 units. Also, less than 5% of the AlO_4 units share edges with other AlO_4 units (Table III), which means that the majority of these doubly shared oxygen atoms should correspond to ordinary corner-sharing connections between two tetrahedra. Figure 9 shows a schematic of the major polyhedral connection types based on this information.

C. Distortion of the polyhedral units

To investigate the effect of the high oxygen atom connectivity on the regularity of the polyhedral units, the partial pair-distribution functions $g_{\text{Al}_x\text{O}}(r)$ were investigated for the RMC model. As shown in Fig. 10, the first peak in $g_{\text{Al4O}}(r)$ at 1.78 Å is sharper and more symmetric than the first peak in $g_{\text{Al5O}}(r)$ at 1.83 Å. The high- r tail to the first peak in the overall Al-O partial pair-distribution function $g_{\text{AlO}}(r)$ therefore has a larger contribution in the range 2.1–2.5 Å from $g_{\text{Al5O}}(r)$, indicating that Al5-type units have a wider range of Al-O bond distances than Al4-type units. For comparison, in the andalusite polymorph of Al_2SiO_5 , the Si atoms are fourfold coordinated and the Al atoms are either five- or sixfold coordinated.^{97–99} Under ambient conditions, the AlO_5 units form distorted trigonal bipyramids that share a common edge with four Al-O bonds in the range 1.81–1.84 Å and a longer Al-O bond at 1.89 Å whose length is relatively more temperature dependent.⁹⁷

Further splitting of $g_{\text{Al4O}}(r)$ into its contributions from $g_{\text{Al4O2}}(r)$ and $g_{\text{Al4O3}}(r)$, where the O2 and O3 oxygen atoms are predominantly twofold or threefold coordinated, respectively, reveals a nearly symmetric first peak in $g_{\text{Al4O2}}(r)$ centered on 1.76 Å, with only a small tail at distances greater than 2.1 Å, as expected for regular corner-sharing tetrahedra (Fig. 10). In comparison, the first peak in $g_{\text{Al4O3}}(r)$ occurs at a longer distance of 1.79 Å and has a notable high- r tail in the 2.1–2.4 Å region. This indicates that the packing constraints associated with the formation of oxygen triclusters lead to a greater distortion of the tetrahedral units.

To investigate the distortion of the AlO_5 polyhedra, it is convenient first to consider square pyramidal and trigonal bipyramidal units, which can be easily interconverted by a reorientation of axes.¹⁰⁰ For a regular square pyramidal

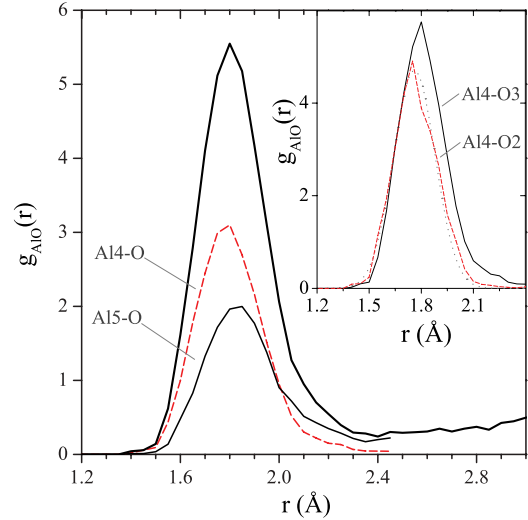


FIG. 10. (Color online) The partial pair-distribution function $g_{\text{AlO}}(r)$ obtained from the RMC model (thick solid (black) curve) and its contributions from $g_{\text{Al4O}}(r)$ (broken (red) curve) and $g_{\text{Al5O}}(r)$ (solid (black) curve). The inset shows the further breakdown of $g_{\text{Al4O}}(r)$ into its contributions from $g_{\text{Al4O2}}(r)$ and $g_{\text{Al4O3}}(r)$, where the predominantly tetrahedral Al4-type units are linked either by predominantly threefold coordinated oxygen atoms O3 corresponding to oxygen triclusters (solid (black) curve) or by predominantly twofold coordinated oxygen atoms O2 (broken (red) curve). The dotted (gray) curve is a Gaussian drawn to highlight the symmetry of the first peak in $g_{\text{Al4O2}}(r)$. By comparison, the first peak in $g_{\text{Al4O3}}(r)$, associated with predominantly threefold coordinated oxygen atoms, is more asymmetric in that it has a high- r tail.

conformation with equal O-O distances, the Al-O distances are equal if the Al atom is placed at the center of the base, and the three intrapolyhedral O-Al-O angles are $\alpha' = 90^\circ$, $\beta' = 90^\circ$, and $\gamma' = 180^\circ$ with relative weightings of 4, 4, and 2, respectively (Fig. 11). Alternatively, if the Al atom is displaced toward the apex by a distance $h/5$, where h is the base-to-apex distance (this configuration gives the unit a zero dipole moment), then four of the Al-O distances are $1.02h$, the other is $0.8h$, and the intrapolyhedral angles become $\alpha' = 87.80^\circ$, $\beta' = 101.31^\circ$, and $\gamma' = 157.38^\circ$. Also, if the Al is kept at a distance $h/5$ above the base but h is now elongated to give equal Al-O distances, the intrapolyhedral angles become $\alpha' = 86.42^\circ$, $\beta' = 104.48^\circ$, and $\gamma' = 151.04^\circ$. By comparison, if the Al atom is placed in the center of a regular trigonal bipyramid with equal O-O distances, then two of the Al-O distances are greater than the other three by a factor of $\sqrt{2}$, and the intrapolyhedral O-Al-O angles are $\alpha = 90^\circ$, $\beta = 120^\circ$, and $\gamma = 180^\circ$ with relative weightings of 6, 3, and 1, respectively (Fig. 11).

Visual inspection of the MD and RMC models showed significant distortion of the AlO_5 polyhedra with a variety of conformations, ranging from broadly trigonal bipyramidal to square pyramidal. This observation was confirmed for the RMC model by calculating the intrapolyhedral O-Al $_x$ -O and interpolyhedral Al $_x$ -O-Al $_x$ bond-angle distributions $B(\theta)$, which are plotted in Fig. 11 as $B(\theta)/\sin\theta$ in order to remove the effect of the finite sampling volume such that a peak at $\theta \cong 180^\circ$ will not, e.g., be artificially suppressed.¹⁰¹ As

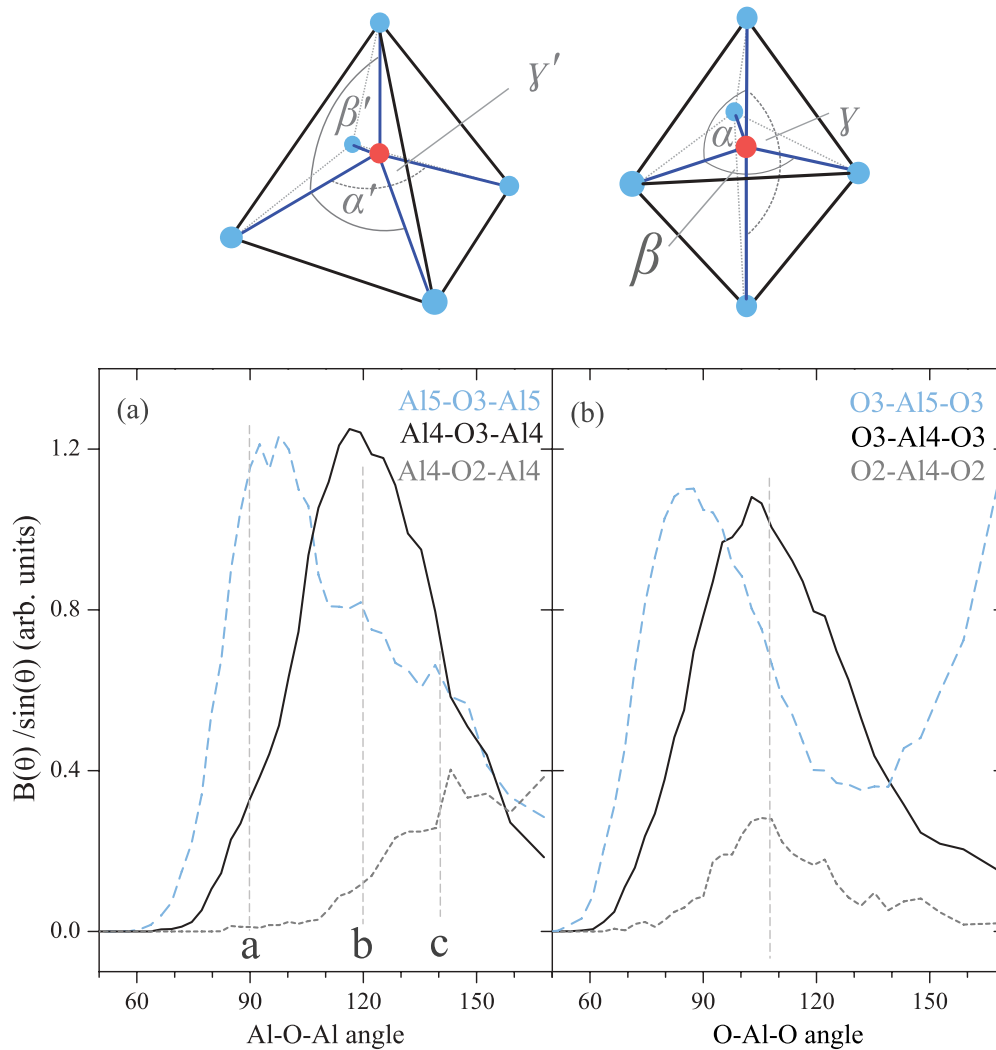


FIG. 11. (Color online) Top: Sketches of the square pyramidal (left) and trigonal bipyramidal (right) AlO_5 configurations, where the intrapolyhedral angles are denoted by α' , β' , and γ' or α , β , and γ , respectively. Bottom: Several of the (a) interpolyhedral Al-O-Al and (b) intrapolyhedral O-Al-O bond-angle distributions obtained from the RMC model. In (a), the Al5-O3-Al5 (broken (blue) curve), Al4-O3-Al4 (solid (black) curve), and Al4-O2-Al4 (broken (gray) curve) bond-angle distributions are given, where O2 and O3 represent predominantly twofold and threefold coordinated oxygen atoms, respectively. The vertical broken lines labeled *a*, *b*, and *c* indicate the approximate angles corresponding to three main features of the liquid structure, namely, $a \approx 90^\circ$ for edge-sharing AlO_5 - AlO_5 or AlO_5 - AlO_4 connections, $b \approx 120^\circ$ for threefold coordinated oxygen atoms linked to three AlO_4 / AlO_5 units by their corners, and $c \approx 140^\circ$ for twofold coordinated oxygen atoms linked to two AlO_4 tetrahedra by their corners. In (b), the O3-Al5-O3 (broken (blue) curve), O3-Al4-O3 (solid (black) curve), and O2-Al4-O2 (short broken (gray) curve) bond-angle distributions are given, and the vertical broken line corresponds to the intratetrahedral angle of 109.47° .

discussed in Sec. VB, the majority, or 91(1)%, of the oxygen atoms in Al5-type units are shared among three or more polyhedra such that the O3-Al5-O3 bond-angle distribution accounts for the majority of connections. This bond-angle distribution has a broad main peak at $86(1)^\circ$, with a shoulder in the region 105 – 120° , followed by a steady increase over the region 140 – 170° , in line with the features expected for distorted trigonal bipyramidal and square pyramidal AlO_5 units.

The intratetrahedral O2-Al4-O2 and O3-Al4-O3 bond-angle distributions have peaks at $106(1)^\circ$ and $101(1)^\circ$, respectively, compared to an O-Al-O bond angle of 109.47° for regular tetrahedra (Fig. 11). This indicates that the tetrahedra linked by threefold coordinated oxygen atoms are more

distorted than those linked by twofold coordinated oxygen atoms.

The Al5-O3-Al5 bond-angle distribution describes most connections between two Al5-type units and has a peak at ~ 92 – 98° , consistent with a significant fraction of edge-sharing AlO_5 units, followed by a shoulder in the range 120 – 160° , which is therefore a feature associated with a large fraction of AlO_5 units triply shared by an oxygen corner. In comparison, the small magnitude of the Al4-O3-Al4 bond-angle distribution below 100° supports the formation of only a small number of edge-sharing tetrahedra, while the peak at 116° must be associated with the formation of oxygen triclusters, wherein an oxygen atom is shared among three AlO_4 units. The broad feature in the Al4-O2-Al4 bond-angle distribution starting at

$\sim 120^\circ$ is consistent with the formation of corner-sharing AlO_4 units as observed in systems like glassy GeO_2 (where the peak in the Ge-O-Ge bond-angle distribution is at $\sim 130^\circ$) and SiO_2 (where the peak in the Si-O-Si bond-angle distribution is at $\sim 150^\circ$).^{81,102,103}

VI. CONCLUSIONS

The structure of liquid Al_2O_3 close to its melting point was investigated using neutron and x-ray diffraction, and a detailed atomistic model was constructed using RMC to refine the MD model of Du and Corrales,⁶¹ which was already in good agreement with the experimental results. From the RMC model we find that although the exact ratio of AlO_4 to AlO_5 polyhedra depends on the precise value chosen for the cutoff distance r_{cut} due to the presence of a large- r tail in $g_{\text{AlO}}(r)$, roughly 2/3 of the structural units are AlO_4 tetrahedra and 1/3 of the structural units are AlO_5 polyhedra. Only small fractions of AlO_3 and AlO_6 polyhedra could be found. This model for the liquid, in which AlO_4 tetrahedra are the predominant structural motifs, is consistent with the available NMR data.^{49–52} Thus, the density decrease of 20–24% on melting the thermodynamically stable crystal structure of $\alpha\text{-Al}_2\text{O}_3$ (Refs. 14 and 43) is accompanied by a breakdown of octahedral AlO_6 motifs.

The AlO_x units are highly connected with 81(2)% of the oxygen atoms linked to three or more polyhedra. The majority of these oxygen atoms are triply shared among one or two AlO_4 units and two or one AlO_5 units, consistent with the abundance of these polyhedra in the melt and their fairly uniform spatial distribution. This absence of clustering for like-type structural motifs at ambient pressure contrasts with a previous report³⁴ and does not suggest the vicinity of a first-order liquid–liquid phase transition. The majority of Al-O-Al connections involve corner-sharing polyhedra (83%), although there is a significant minority of edge-sharing polyhedra (16%). Of the latter, $\sim 1/3$ of the AlO_5 - AlO_5 units share edges compared to $\sim 1/6$ of the AlO_5 - AlO_4 units. The geometry of the AlO_5 units ranges from trigonal bipyramidal to square pyramidal. The nature of the structural units and their connectivity in the liquid

accounts for the absence of glass formation in Al_2O_3 , in accordance with Zachariassen's rules,¹⁰⁴ since (1) many of the oxygen atoms are linked to more than two Al atoms, (2) a significant fraction of Al atoms have a coordination number in excess of four, and (3) many of the structural motifs share edges. However, when mixed with materials like CaO, the liquid becomes a fragile glass former, where the temperature dependence of the viscosity is likely to be linked to several of the topological features found in liquid Al_2O_3 , such as edge-sharing Al-centered polyhedra and threefold coordinated oxygen atoms.^{105–107}

ACKNOWLEDGMENTS

We thank the Engineering and Physical Sciences Research Council (EPSRC) for financial support. L.B.S. thanks the EPSRC and the US Department of Energy for support (Grant No. DE-FG02-09ER46650). We also thank Pierre Palleau at the ILL for his assistance with the neutron diffraction experiment, Rick Spence at the APS for assistance with the x-ray diffraction experiment, Jincheng Du for useful discussions, and Sandro Jahn for supplying the relative fractions of OAl_x species for the model described in Ref. 53. This work was also supported by the US Department of Energy, Basic Energy Sciences, Office of Science, under Contract No. DE-AC02-06CH11357. The synchrotron radiation experiments at SPring-8 were approved by the Japan Synchrotron Radiation Research Institute (Proposal Nos. 2006A1200, 2010B2015, 2011A2051, and 2011A1103). S.K. and K.O. thank Masahito Watanabe, Akitoshi Mizuno, and Jumpei Yahiro for helping to develop the aerodynamic levitation apparatus at SPring-8. P.S.S. thanks Andy Moskalenko for translating the papers in Russian.

The experiments were made by L.B.S., C.J.B., J.K.R.W., J.B.P., and S.K.T. (APS); L.B.S., A.C.B., L.H., A.B., I.P., and P.S.S. (ESRF); L.B.S., L.H., H.E.F., and T.O.F. (ILL); and S.K. and K.O. (SPring-8). The most significant contributions to the manuscript were made by P.S.S., L.B.S., A.C.B., H.E.F., C.J.B., S.K., J.K.R.W., and M.C.W.

¹I. Levin and D. Brandon, *J. Am. Ceram. Soc.* **81**, 1995 (1998).

²B. Cockayne, M. Chesswas, and D. B. Gasson, *J. Mater. Sci.* **2**, 7 (1967).

³H. E. LaBelle, Jr., and A. I. Mlavsky, *Mater. Res. Bull.* **6**, 571 (1971).

⁴H. E. LaBelle, Jr., *Mater. Res. Bull.* **6**, 581 (1971).

⁵M. M. Fejer, J. L. Nightingale, G. A. Magel, and R. L. Byer, *Rev. Sci. Instrum.* **55**, 1791 (1984).

⁶R. K. Nubling and J. A. Harrington, *Appl. Opt.* **36**, 5934 (1997).

⁷R. A. Reed and V. S. Calia, AIAA Paper No. 93-2819 (American Institute of Aeronautics and Astronautics, Washington, DC, 1993).

⁸Yu. Plastinin, G. Karabadzhak, B. Khmelinin, G. Baula, and A. Rodionov, AIAA Paper No. 2001-0660 (American Institute of Aeronautics and Astronautics, Reston, VA, 2001).

⁹J. M. Burt and I. D. Boyd, *AIAA J.* **45**, 2872 (2007).

¹⁰S. J. Schneider, *Pure Appl. Chem.* **21**, 115 (1970).

¹¹V. P. Elyutin, B. S. Mitin, and Yu. S. Anisimov, *Izv. Akad. Nauk. SSSR Neorg. Mater.* **9**, 1585 (1973).

¹²M. A. Maurakh, B. S. Mitin, and M. B. Roitberg, *Zavod. Lab.* **33**, 984 (1967).

¹³W. D. Kingery, *J. Am. Ceram. Soc.* **42**, 6 (1959).

¹⁴J. J. Rasmussen, *J. Am. Ceram. Soc.* **55**, 326 (1972).

¹⁵A. D. Kirshenbaum and J. A. Cahill, *J. Inorg. Nucl. Chem.* **14**, 283 (1960).

¹⁶B. S. Mitin and Yu. A. Nagibin, *Russ. J. Phys. Chem.* **44**, 741 (1970); *Zh. Fiz. Khim.* **44**, 1325 (1970).

¹⁷N. Ikemiya, J. Umamoto, S. Hara, and K. Ogino, *ISIJ Int.* **33**, 156 (1993).

¹⁸E. E. Shpil'rain, K. A. Yakimovich, and A. F. Tsitsarkin, *High Temp. High Press.* **5**, 191 (1973).

¹⁹B. Glorieux, F. Millot, J.-C. Rifflet, and J.-P. Coutures, *Int. J. Thermophys.* **20**, 1085 (1999).

- ²⁰B. Granier and S. Heurtault, *Rev. Int. Hautes Tempér. Réfract. Fr.* **20**, 61 (1983).
- ²¹J.-P. Coutures, J.-Cl. Rifflet, P. Florian, and D. Massiot, *Rev. Int. Hautes Tempér. Réfract. Fr.* **29**, 123 (1994).
- ²²P.-F. Paradis, T. Ishikawa, Y. Saita, and S. Yoda, *Jpn. J. Appl. Phys.* **43**, 1496 (2004).
- ²³P. C. Nordine, J. K. R. Weber, and J. G. Abadie, *Pure Appl. Chem.* **72**, 2127 (2000).
- ²⁴G. R. Helffrich and B. J. Wood, *Nature* **412**, 501 (2001).
- ²⁵J.-P. Poirier, *Introduction to the Physics of the Earth's Interior*, 2nd ed. (Cambridge University Press, Cambridge, UK, 2000).
- ²⁶J. L. Yarger, K. H. Smith, R. A. Nieman, J. Diefenbacher, G. H. Wolf, B. T. Poe, and P. F. McMillan, *Science* **270**, 1964 (1995).
- ²⁷J. R. Allwardt, J. F. Stebbins, B. C. Schmidt, D. J. Frost, A. C. Withers, and M. M. Hirschmann, *Am. Mineral.* **90**, 1218 (2005).
- ²⁸E. Ohtani, F. Taulelle, and C. A. Angell, *Nature* **314**, 78 (1985).
- ²⁹A. E. Ringwood, A. F. Reid, and A. D. Wadsley, *Acta Crystallogr.* **23**, 1093 (1967).
- ³⁰G. N. Greaves, M. C. Wilding, S. Fearn, D. Langstaff, F. Kargl, S. Cox, Q. V. Van, O. Majérus, C. J. Benmore, R. Weber, C. M. Martin, and L. Hennet, *Science* **322**, 566 (2008).
- ³¹A. C. Barnes, L. B. Skinner, P. S. Salmon, A. Bytchkov, I. Pozdnyakova, T. O. Farmer, and H. E. Fischer, *Phys. Rev. Lett.* **103**, 225702 (2009).
- ³²G. N. Greaves, M. C. Wilding, L. Hennet, D. Langstaff, F. Kargl, C. J. Benmore, and J. K. R. Weber, *Phys. Rev. Lett.* **106**, 119601 (2011).
- ³³A. C. Barnes, L. B. Skinner, P. S. Salmon, A. Bytchkov, I. Pozdnyakova, T. O. Farmer, and H. E. Fischer, *Phys. Rev. Lett.* **106**, 119602 (2011).
- ³⁴M. Hemmati, M. Wilson, and P. A. Madden, *J. Phys. Chem. B* **103**, 4023 (1999).
- ³⁵V. V. Hoang and S. K. Oh, *Phys. Rev. B* **72**, 054209 (2005).
- ³⁶A. K. Verma, P. Modak, and B. B. Karki, *Phys. Rev. B* **84**, 174116 (2011).
- ³⁷V. V. Hoang, *Phys. Lett. A* **335**, 439 (2005).
- ³⁸P. K. Hung, L. T. Vinh, D. M. Nghiep, and P. N. Nguyen, *J. Phys. Condens. Matter* **18**, 9309 (2006).
- ³⁹P.-F. Paradis and T. Ishikawa, *Jpn. J. Appl. Phys.* **44**, 5082 (2005).
- ⁴⁰J. E. Enderby, S. Ansell, S. Krishnan, D. L. Price, and M.-L. Saboungi, *Appl. Phys. Lett.* **71**, 116 (1997).
- ⁴¹H. Sinn, B. Glorieux, L. Hennet, A. Alatas, M. Hu, E. E. Alp, F. J. Bermejo, D. L. Price, and M.-L. Saboungi, *Science* **299**, 2047 (2003).
- ⁴²S. Krishnan, J. K. R. Weber, R. A. Schiffman, P. C. Nordine, and R. A. Reed, *J. Am. Ceram. Soc.* **74**, 881 (1991).
- ⁴³P. Tyrolerova and W.-K. Lu, *J. Am. Ceram. Soc.* **52**, 77 (1969).
- ⁴⁴S. Ansell, S. Krishnan, J. K. R. Weber, J. J. Felten, P. C. Nordine, M. A. Beno, D. L. Price, and M.-L. Saboungi, *Phys. Rev. Lett.* **78**, 464 (1997).
- ⁴⁵L. Hennet, D. Thiaudière, M. Gailhanou, C. Landron, J.-P. Coutures, and D. L. Price, *Rev. Sci. Instrum.* **73**, 124 (2002).
- ⁴⁶S. Kohara, M. Itou, K. Suzuya, Y. Inamura, Y. Sakurai, Y. Ohishi, and M. Takata, *J. Phys. Condens. Matter* **19**, 506101 (2007).
- ⁴⁷S. Krishnan, L. Hennet, S. Jahn, T. A. Key, P. A. Madden, M.-L. Saboungi, and D. L. Price, *Chem. Mater.* **17**, 2662 (2005).
- ⁴⁸C. Landron, L. Hennet, T. E. Jenkins, G. N. Greaves, J. P. Coutures, and A. K. Soper, *Phys. Rev. Lett.* **86**, 4839 (2001).
- ⁴⁹J.-P. Coutures, D. Massiot, C. Bessada, P. Echegut, J.-C. Rifflet, and F. Taulelle, *C. R. Acad. Sci. Paris.* **310**, 1041 (1990).
- ⁵⁰D. Massiot, F. Taulelle, and J. P. Coutures, *J. Phys. Coll.* **51**, C5-425 (1990).
- ⁵¹B. T. Poe, P. F. McMillan, B. Coté, D. Massiot, and J.-P. Coutures, *J. Phys. Chem.* **96**, 8220 (1992).
- ⁵²P. Florian, D. Massiot, B. Poe, I. Farnan, and J.-P. Coutures, *Solid State Nucl. Magn. Reson.* **5**, 233 (1995).
- ⁵³S. Jahn and P. A. Madden, *J. Non-Cryst. Solid.* **353**, 3500 (2007).
- ⁵⁴V. V. Hoang and S. K. Oh, *J. Phys. Condens. Matter* **17**, 3025 (2005).
- ⁵⁵G. Gutiérrez, A. B. Belonoshko, R. Ahuja, and B. Johansson, *Phys. Rev. E* **61**, 2723 (2000).
- ⁵⁶M. A. S. Miguel, J. F. Sanz, L. J. Álvarez, and J. A. Odriozola, *Phys. Rev. B* **58**, 2369 (1998).
- ⁵⁷R. Ahuja, A. B. Belonoshko, and B. Johansson, *Phys. Rev. E* **57**, 1673 (1998).
- ⁵⁸P. Vashishta, R. K. Kalia, A. Nakano, and J. P. Rino, *J. Appl. Phys.* **103**, 083504 (2008); **105**, 059901 (2009).
- ⁵⁹A. K. Soper, *Chem. Phys.* **202**, 295 (1996).
- ⁶⁰Y. Waseda, K. Sugiyama, and J. M. Toguri, *Z. Naturforsch. A Phys. Sci.* **50**, 770 (1995).
- ⁶¹J. Du and L. R. Corrales, *J. Non-Cryst. Solid.* **353**, 210 (2007).
- ⁶²J. Du, C. J. Benmore, R. Corrales, R. T. Hart, and J. K. R. Weber, *J. Phys. Condens. Matter* **21**, 205102 (2009).
- ⁶³A. Winkler, J. Horbach, W. Kob, and K. Binder, *J. Chem. Phys.* **120**, 384 (2004).
- ⁶⁴R. L. McGreevy and L. Pusztai, *Mol. Simul.* **1**, 359 (1988).
- ⁶⁵L. B. Skinner, A. C. Barnes, P. S. Salmon, H. E. Fischer, J. W. E. Drewitt, and V. Honkimäki, *Phys. Rev. B* **85**, 064201 (2012).
- ⁶⁶H. E. Fischer, A. C. Barnes, and P. S. Salmon, *Rep. Prog. Phys.* **69**, 233 (2006).
- ⁶⁷H. Rauch and W. Waschkowski, in *Neutron Data Booklet*, 2nd ed., edited by A.-J. Dianoux and G. Lander (Old City Publishing Group, Philadelphia, 2003), Chap. 1-1.
- ⁶⁸J. H. Hubbell and I. Øverbø, *J. Phys. Chem. Ref. Data* **8**, 69 (1979).
- ⁶⁹E. Lorch, *J. Phys. C Solid State Phys.* **2**, 229 (1969).
- ⁷⁰The mathematical validity of the Lorch function has been called into question in Ref. 71. However, a rigorous derivation, which also gives an analytical expression for the real-space manifestation of this function, is given in Ref. 72.
- ⁷¹A. K. Soper and E. R. Barney, *J. Appl. Crystallogr.* **44**, 714 (2011).
- ⁷²P. S. Salmon, *J. Phys. Condens. Matter* **18**, 11443 (2006).
- ⁷³A. Zeidler, J. W. E. Drewitt, P. S. Salmon, A. C. Barnes, W. A. Crichton, S. Klotz, H. E. Fischer, C. J. Benmore, S. Ramos, and A. C. Hannon, *J. Phys.: Condens. Matter* **21**, 474217 (2009).
- ⁷⁴L. Hennet, I. Pozdnyakova, A. Bytchkov, V. Cristiglio, P. Palleau, H. E. Fischer, G. J. Cuello, M. Johnson, P. Melin, D. Zanghi, S. Brassamin, J.-F. Brun, D. L. Price, and M.-L. Saboungi, *Rev. Sci. Instrum.* **77**, 053903 (2006).
- ⁷⁵J. K. R. Weber, S. Krishnan, C. D. Anderson, and P. C. Nordine, *J. Am. Ceram. Soc.* **78**, 583 (1995).
- ⁷⁶J.-C. Labiche, O. Mathon, S. Pascarelli, M. A. Newton, G. G. Ferre, C. Curfs, G. Vaughan, A. Homs, and D. F. Carreiras, *Rev. Sci. Instrum.* **78**, 091301 (2007).
- ⁷⁷A. P. Hammersley, S. O. Svensson, M. Hanfland, A. N. Fitch, and D. Häusermann, *High Pressure Res.* **14**, 235 (1996).
- ⁷⁸L. B. Skinner, C. J. Benmore, and J. B. Parise, *Nucl. Instrum. Methods Phys. Res. A* **662**, 61 (2012).
- ⁷⁹H. E. Fischer, G. J. Cuello, P. Palleau, D. Felten, A. C. Barnes, Y. S. Badyal, and J. M. Simonson, *Appl. Phys. A* **74**, S160 (2002).

- ⁸⁰W. Smith and T. R. Forester, *J. Mol. Graphics* **14**, 136 (1996).
- ⁸¹P. S. Salmon, A. C. Barnes, R. A. Martin, and G. J. Cuello, *J. Phys. Condens. Matter* **19**, 415110 (2007).
- ⁸²P. S. Salmon, R. A. Martin, P. E. Mason, and G. J. Cuello, *Nature* **435**, 75 (2005).
- ⁸³P. S. Salmon, A. C. Barnes, R. A. Martin, and G. J. Cuello, *Phys. Rev. Lett.* **96**, 235502 (2006).
- ⁸⁴I. Petri, P. S. Salmon, and H. E. Fischer, *Phys. Rev. Lett.* **84**, 2413 (2000).
- ⁸⁵C. J. Benmore, J. K. R. Weber, S. Sampath, J. Siewenie, J. Urquidi, and J. A. Tangeman, *J. Phys. Condens. Matter* **15**, S2413 (2003).
- ⁸⁶L. B. Skinner, A. C. Barnes, and W. Crichton, *J. Phys. Condens. Matter* **18**, L407 (2006).
- ⁸⁷M. C. Wilding, C. J. Benmore, and J. K. R. Weber, *J. Phys. Chem. B* **114**, 5742 (2010).
- ⁸⁸Q. Mei, C. J. Benmore, J. K. R. Weber, M. Wilding, J. Kim, and J. Rix, *J. Phys. Condens. Matter* **20**, 245107 (2008).
- ⁸⁹R. A. Martin, P. S. Salmon, D. L. Carroll, M. E. Smith, and A. C. Hannon, *J. Phys. Condens. Matter* **20**, 115204 (2008).
- ⁹⁰A. Pedone, G. Malavasi, M. C. Menziani, A. N. Cormack, and U. Segre, *J. Phys. Chem. B* **110**, 11780 (2006).
- ⁹¹M. Matsui, *Phys. Chem. Miner.* **23**, 345 (1996).
- ⁹²P. A. Madden and M. Wilson, *Chem. Soc. Rev.* **25**, 339 (1996).
- ⁹³S. Jahn, P. A. Madden, and M. Wilson, *Phys. Rev. B* **74**, 024112 (2006).
- ⁹⁴S. K. Lee, S. B. Lee, S. Y. Park, Y. S. Yi, and C. W. Ahn, *Phys. Rev. Lett.* **103**, 095501 (2009).
- ⁹⁵P. S. Salmon, *Proc. R. Soc. Lond. A* **437**, 591 (1992).
- ⁹⁶A. B. Bhatia and D. E. Thornton, *Phys. Rev. B* **2**, 3004 (1970).
- ⁹⁷J. K. Winter and S. Ghose, *Am. Mineral.* **64**, 573 (1979).
- ⁹⁸R. L. Ralph, L. W. Finger, R. M. Hazen, and S. Ghose, *Am. Mineral.* **69**, 513 (1984).
- ⁹⁹J. B. Burt, N. L. Ross, R. J. Angel, and M. Koch, *Am. Mineral.* **91**, 319 (2006).
- ¹⁰⁰A. Pasquarello, I. Petri, P. S. Salmon, O. Parisel, R. Car, E. Tóth, D. H. Powell, H. E. Fischer, L. Helm, and A. E. Merbach, *Science* **291**, 856 (2001).
- ¹⁰¹A. Zeidler, P. S. Salmon, R. A. Martin, T. Usuki, P. E. Mason, G. J. Cuello, S. Kohara, and H. E. Fischer, *Phys. Rev. B* **82**, 104208 (2010).
- ¹⁰²S. Kohara and K. Suzuya, *J. Phys. Condens. Matter* **17**, S77 (2005).
- ¹⁰³A. C. Wright, *J. Non-Cryst. Solid.* **179**, 84 (1994).
- ¹⁰⁴W. H. Zachariasen, *J. Am. Chem. Soc.* **54**, 3841 (1932).
- ¹⁰⁵M. Wilson and P. S. Salmon, *Phys. Rev. Lett.* **103**, 157801 (2009).
- ¹⁰⁶J. W. E. Drewitt, S. Jahn, V. Cristiglio, A. Bytchkov, M. Leydier, S. Brassamin, H. E. Fischer, and L. Hennet, *J. Phys. Condens. Matter* **23**, 155101 (2011).
- ¹⁰⁷J. W. E. Drewitt, L. Hennet, A. Zeidler, S. Jahn, P. S. Salmon, D. R. Neuville, and H. E. Fischer, *Phys. Rev. Lett.* **109**, 235501 (2012).